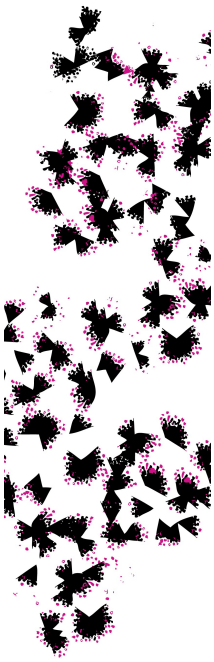

Controller design for Dual-Hemi CVT

A.(Armando) Bonilla Fernandez

MSc Report

Committee:
Prof.dr.ir. S. Stramigioli
D. Dresscher, MSc
Dr.ir. T.J.A. de Vries
Dr.ir. J. van Dijk

August 2016

026RAM2016
Robotics and Mechatronics
EE-Math-CS
University of Twente
P.O. Box 217
7500 AE Enschede
The Netherlands

Summary

The aim of this assignment was to design a controller for the reconfiguration mechanism of the Dual-Hemi CVT. To do this, first, an ideal model of the system was developed. The first modelling approach that was used was an IPM, because of the intuitiveness of representing the system based on the mechanical connections. This also helped to understand and gain insight of the functionality of the setup. In order to obtain information about the energy flow and the dependency of the different components in the system, the port-based approach was used to generate a *bond-graph* model. At the beginning, all the elements in the bond-graph were considered as ideal, and based this premise, this model was used to identify all the torques that were caused by non idealities in the mechanism. This non idealities are attributed to the torques generated due to friction and spring residual forces. As a result of the identification, it was possible to observe that the non ideal behavior had a dependency with the position and velocity of the mechanism. Functions that approximately resemble this non ideal behavior were obtained, and combined together with the equations that describe the ideal behavior of the gravity compensator's residual forces. This created a *feed forward controller*. It is important to notice that, since the functions for the non idealities are continuous, it is quite hard to compensate throughout all the different force values. Nonetheless, results showed that the estimation is quite good and capable of robustly compensate for these disturbances.

Once a functional adaptive feed forward was developed, it was possible to consider the reconfiguration mechanism as an ideal plant. This makes the procedure for the feedback control design easier. At this stage of the project, we designed three different controllers using two different PID algorithms. First a series PID was designed based on the rules of thumb explained in Section 2.3.1.2. Using simulations tools, such as 20-sim, we observed that this controller had very high gains for low frequencies that lead to rough behavior, i.e. very high overshoot (such as hitting the end stops). Because of this, the controller was tuned, to limit the gain. After this adjustment, simulations showed that controller's performance was vastly improved. The second approach used the parallel PID algorithm, which was designed using a pragmatic procedure, as described in Section 4.2.3. In simulations, the observed response of this controller was very good, presenting an overdamped system but with very fast response.

With these three controller candidates, several experiments were run in the setup, which are described in Chapter 5. Given the fact that one of the considerations for selecting the controller was the energy efficiency of the whole system, it was found that the second series PID presented the best results.

Contents

1 Introduction

1.1 Context

In the Netherlands dikes are of great importance for flooding prevention, since large part of the territory is below sea level. Nonetheless, their inspection requires a labor intensive network of trained people. Because of this, the RObotic SEnsor (ROSE) project aims to develop a team of walking robotic sensors that will autonomously inspect dikes [1]. Walking robots are preferred because they are able to cope with non-smooth (steep slopes) and muddy environments,. However, low energy efficiency lost in acceleration and deceleration during walking, presents a problem to use them in such operations, due to the limited supply of power. A solution for this would be to keep the energy flow in the mechanical domain. For this, an energy-efficient transmission is combined with a energy storage element (spring) to drive the walking mechanism. By using such construction, the energy that would otherwise be dissipated (lost), is stored for re-injection in the system during the consecutive steps, as shown in Figure 1.1.

The proposal of the ROSE project is to develop a system to temporarily store the kinetic energy that would otherwise be lost. The storage can e.g. be done with a spring. This energy would then be used for the actuation of the following steps. For this reason, a system that can vary the transmission ratio between the storage element (spring) and payload force was developed. Many proposed design concepts were analyzed for the implementation of this hypothesis, from which a dual-hemispherical variable transmission was chosen. This system was called the Dual-Hemi CVT and it is composed of two sphere shaped friction wheels which transfer force due to friction between them. By alternating the angle at which both spheres are positioned with respect to each other, the transmission ratio can be adjusted [1].

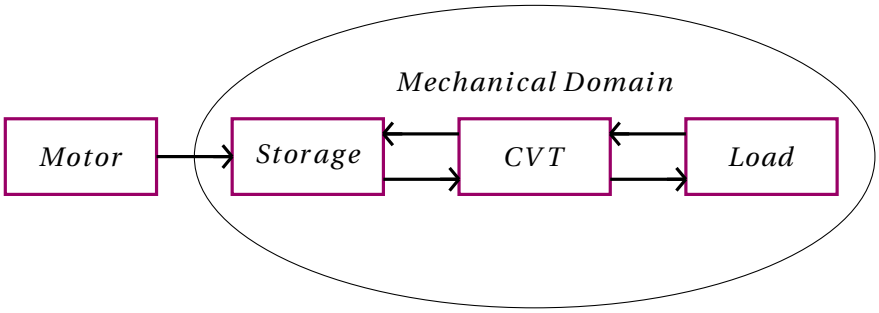

Figure 1.1: Energy flow diagram, where the arrow represent the flow direction

1.2 Problem statement

Up until recently, in the Dual-Hemi CVT, considerable attention has been paid to the performance of the mechanical path that transmits the power, i.e. from input (spring force) to output (system's load). This has currently resulted in an overall efficiency between 90% and 100% for the majority of the operational range. However, more optimization for the performance is desired. The bandwidth of the whole mechanism (DH-CVT) is mainly dependent on the bandwidth of the system that changes the transmission ratio, i.e. the *reconfiguration mechanism*, which according to [2] has a bandwidth $\approx 17\ rad/s$. In order to improve the bandwidth and therewith the performance, a closer study of this part of the system is required.

1.3 Approach

The work described in this report proposes to make a deeper analysis of the reconfiguration mechanism and, with the gained insight, improve its performance. This project will first

develop a comprehensive model of the reconfiguration mechanism. To start, an IPM representation is chosen based on the insight that it offers on the mechanical connections between the parts as well as the fact that it provides an easier way of simplification compared to other approaches. After simplification is completed, the model is represented into the preferred port-based approach where deeper analysis of the dynamics can be carried out. Once a model formed by ideal elements is obtained, it is tested with respect the real setup conditions, to determine its competence. At this stage, all non-identifiable behavior between the model and the setup will be represented as a single element in the model. With a competent model (including the residual and friction forces), a feed-forward controller, needed to compensate the residual and friction generated forces, can already be developed. Thus, for the feedback controller design, the plant will considered as a system without residual and friction forces. To develop this last controller, two design approaches will be explored, in order to compare their performances and make the choice for the best alternative. The combination of the feed forward and feedback controller will lead to a robust servomechanism (good tracking and small steady state error), and with a crossover frequency of 100 rad/s. This, because it is desired to have a fast response from our system and also keep the sample frequency of the controller in a relative low range to avoid computational problems.

1.4 Organization of the Report

In chapter 2 theoretical background and earlier work will be introduced, to review and discuss useful concepts as well as to build up a list of requirements needed for the assignment. After that, in chapter 3, the modelling procedure will be explained starting from the IPM representation, continuing with the port-based approach and reviewing the simplification decisions that were taken. Also in this section, model simulations will be presented as well as the analysis resulting of the comparison with the setup, in which non-idealities were found. In chapter 4, the two chosen controller design approaches and their implementation will be explained. In chapter 5, both controller's performances will be compared and results will be discussed. Finally, chapter 6 concludes this thesis and presents recommendations for future developments.

2 Background

This chapter provides a brief background on the topics that will be used throughout the present work. First, it explains the plant modelling process, including the reduction procedure and the fourth-order plant concept. Next a short introduction of the port-based modelling approach is given. Additionally, the concept of motion controllers is described and the two approaches that will be used for feedback controller design are explained. Then, the notion of CPA (Control Passive Actuation) is briefly described. Finally background information on the design and functionality of the Dual-Hemi CVT is provided.

2.1 Plant modelling

A model consists of a graphical or mathematical representation of a system (i.e. the plant). It can be used to analyze and understand the system's dynamics. There exist many different approaches for modelling, nevertheless, throughout the present work two particular ones will be considered: Ideal physical model (IPM) representation and port-based modelling (bond graphs). The first one was used, because it provides a direct graphical representation of the mechanical elements and their interactions. Thus, it was an excellent way to understand the system's behavior at the beginning. The port-based approach, on the other hand, provides a deeper insight on the system's energy flow and is domain independent, therefore, it can represent interactions between the mechanical and electrical domains. Furthermore, in bond graphs, there are established procedures that facilitate the development of mathematical models, representing the system's characteristics in terms of equations so that they can be analyzed with control theory laws.

2.1.1 Model reduction

When obtaining the IPM of a system, at first, all the elements need to be taken into account, however to identify the dominant plant factors, it is advised to make a reduced model, so only this dominant dynamic behavior is analyzed. In order to do this in an IPM, it is desired to eliminate all the transmissions, to compare the magnitude of the elements. Once the transmissions are eliminated the magnitudes are compared, and some elements are excluded. There are two possible criteria, from which only one can be chosen for carrying out the reduction process. The criteria are:

CRITERION 1:

- The masses or inertias that are considerably small compared to the others (≈ 0) are eliminated.
- The stiffnesses with very high values ($\approx \infty$) are considered a rigid connection.

CRITERION 2:

- Masses that are "infinitely inert" ($\approx \infty$) are considered as fixed world.
- Springs that are very compliant ($K \approx 0$) are considered as not connected.

The process of eliminating the transmissions, consists on moving all the elements to one side, adjusting their magnitude according to the transmission ratio. Since, in this project, the goal is to have a model in terms of the end effector, the transmissions are moved towards the input of the system.

Figure 2.1 depicts the graphical displacement of the transmission towards the input (moving to the left side). There, it is possible to observe that m becomes m_t, since its value has been escalated according to the transmission ratio. In order to avoid the loss of information in our

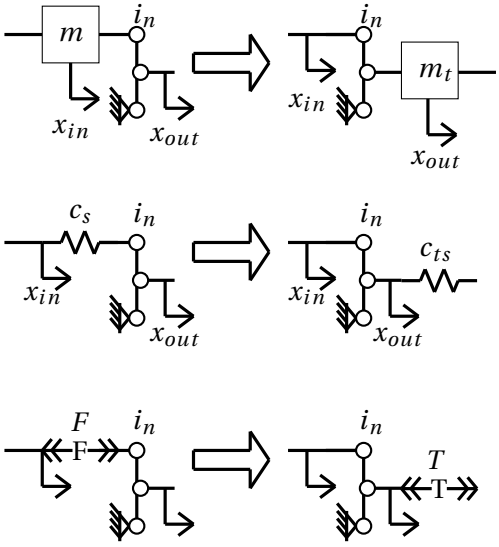

Figure 2.1: Removing transmissions from model

model, it is necessary to keep the same flow of energy when removing transmissions. This can be explained by means of the kinetic energy (co-energy), given by:

$$\frac{1}{2}m\dot{x}_{in}^2 = \frac{1}{2}m_t\dot{x}_{out}^2 \tag{2.1}$$

The value of m_t, i.e. the mass after moving the transmission to the left side, can be obtained using the relation from equation 2.1. Considering the transmission ratio i_n from Fig. 2.1 as the relation "$\dot{x}_{out}/\dot{x}_{in}$", and the substituting this in equation 2.1, it its possible to express the value of m_t as:

$$m_t = \frac{m}{i_n^2} \tag{2.2}$$

In case of springs (stiffness) the same principle applies, if we look at the energy in the spring we obtain the following equation:

$$\frac{1}{2}c_s x_{in}^2 = \frac{1}{2}c_{st}x_{out}^2 \tag{2.3}$$

Where c_s is the spring constant when the spring is located on the left side of the transmission, and c_{st} is the spring constant after moving the element to the right of the transmission. Considering the ratio $i_n = x_{out}/x_{in}$, and then substituting in equation 2.3 and solving the equation for c_{st} we obtain:

$$c_{st} = \frac{c_s}{i_n^2} \tag{2.4}$$

For the sinks and sources we only need to adjust the units in terms of the end effector and scale the value. Thus when a transmission is moved to the left side of a source or sink, it is only necessary to divide by the ratio of the transmission.

$$F = \frac{T}{i_n} \qquad or \qquad T = \frac{F}{i_n} \tag{2.5}$$

2.1.2 Fourth-order plants

According to [3] a fourth order model is a *lumped parameter representation of the dominant dynamic behavior of electromechanical motion system in which only the rigid body mode and the lowest mode of vibrations are taken into account.*

2.1.2.1 Fourth-order transfer functions

In the fourth order model, two positions and their corresponding velocities can be measured and fed back. Depending in which position is measured, a different plant transfer function will result. There are five types of transfer functions at an abstract level [3]. Next, these will be briefly discussed.

2.1.2.1.1 Type AR: Anti-resonance Resonance

In this type of transfer function, the anti-resonance frequency is smaller than the resonance frequency. This means that the zero pair located in the imaginary axis is closer to the origin than the pole pair, as depicted in Figure 2.2.

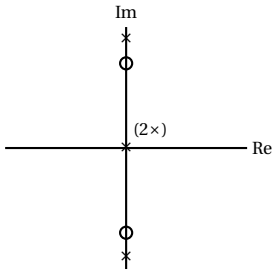

Figure 2.2: Pole-zero map of AR transfer function

The transfer function of type AR is given by:

$$P_{AR}(s) = \frac{1}{ms^2} \cdot \frac{s^2 + \omega_{ar}^2}{s^2 + \omega_r^2} \cdot \frac{\omega_r^2}{\omega_{ar}^2}, \ \omega_{ar} < \omega_r \tag{2.6}$$

2.1.2.1.2 Type D: Double integrator

The transfer function of this type, is equal to the shown in equation 2.6, with $\omega_r = \omega_{ar}$, resulting in equation 2.7:

$$P_D(s) = \frac{1}{ms^2} \tag{2.7}$$

At a first glance, this type seems like the one of a second-order transfer function that is physically related to a mass with an applied force. Nevertheless, the fact that the denominator is of second order relates to the fact that the numerator polynomial apparently has two roots that are identical to two roots of the denominator, causing then a pole-zero cancellation. This is depicted in Figure 2.3.

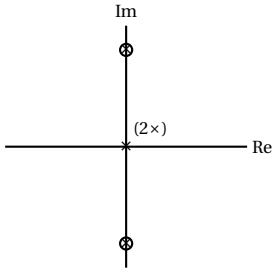

Figure 2.3: Pole-zero map of D transfer function

2.1.2.1.3 Type RA: Resonance- Anti-resonance

This type is comparable to AR, but it presents a different order in which the resonance and anti-resonance peaks appear in the Bode-plot. This means that, in this case, the resonance frequency is smaller then the anti-resonance frequency.

The transfer function of this type is given by:

$$P_{RA}(s) = \frac{1}{ms^2} \cdot \frac{s^2 + \omega_{ar}^2}{s^2 + \omega_r^2} \cdot \frac{\omega_r^2}{\omega_{ar}^2}, \ \omega_{ar} > \omega_r \tag{2.8}$$

In the s-plain this type presents a zero pair in the imaginary axis that is located further away from the origin than the resonance pole pair, as shown in Figure 2.4.

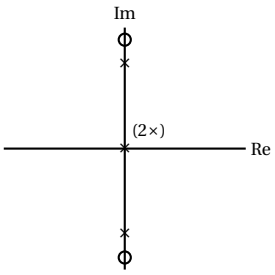

Figure 2.4: Pole-zero map of RA transfer function

2.1.2.1.4 Type R: Resonance

The relevant characteristic of this transfer function type is that it has no zero pair and thus no anti-resonance frequency. This can be observed in Figure 2.5.

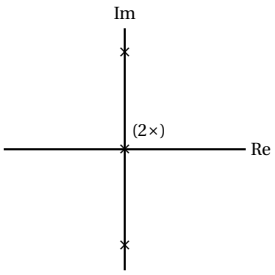

Figure 2.5: Pole-zero map of R transfer function

The type R transfer function is:

$$P_R(s) = \frac{1}{ms^2} \cdot \frac{\omega_r^2}{s^2 + \omega_r^2} \tag{2.9}$$

2.1.2.1.5 Type N: Non-minimum phase

This type's characteristic lays on the fact that it possesses a zero in the right half-plane, as shown in Figure 2.6.

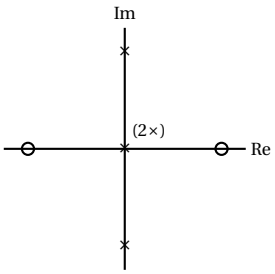

Figure 2.6: Pole-zero map of N transfer function

Because of the presence of this zero, this system is referred to as non-minimum phase. Its equation is given by:

$$P_N(s) = \frac{1}{ms^2} \cdot \frac{s^2 - \omega_{ar}^2}{s^2 + \omega_r^2} \cdot \frac{\omega_r^2}{-\omega_{ar}^2} \tag{2.10}$$

2.1.2.2 Classes of electromechanical motion systems

According to [3] the fourth-order transfer functions mentioned in 2.1.2.1 can be used to describe four classes of electromechanical motion systems. These classes contain the dominant stiffness of the mechanism and are referred to as *standard (fourth-order) plant models* [3]. The four classes are:

1. Flexible mechanism
2. Flexible frame
3. Flexible actuator suspension
4. Flexible guidance

Out of these four classes, the first two relate to a single mechanical domain (rotational or translational), while the last two combine both types of motion (translational and rotational) in the mechanical domain. Since the present work only deals with a single mechanical domain (rotational) only a brief overview of the first two classes will be presented.

2.1.2.2.1 Flexible mechanism

This configuration occurs when the dominant stiffness (c) in the mechanism is located between the mass of the end-effector (m_1) and the mass where the input force is applied (m_2), as depicted in Figure 2.7. This mechanism can be of type AR or of type R, depending on whether the feedback is measured in m_2 or in m_1, respectively. The parameters in this transfer function are:

$$m = m_1 + m_2 \tag{2.11}$$

$$\omega_{ar} = \sqrt{\frac{c}{m_1}} \tag{2.12}$$

$$\omega_r = \sqrt{\frac{c(m_1 + m_2)}{m_1 \cdot m_2}} \tag{2.13}$$

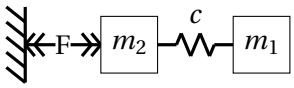

Figure 2.7: Flexible mechanism IPM

2.1.2.2.2 Flexible frame

This configuration occurs when the dominant stiffness (c) in the mechanism is located in the supporting frame (m_2). The other mass (m_1) is a rigid body containing among others the mass of the actuator and the end-effector, as shown in Figure 2.8. The transfer function from the input force to the position measurement with respect to the frame ($y = x_1 - x_2$) is of type AR. The parameters in case the mechanism is of this type are:

$$m = m_1 \tag{2.14}$$

$$\omega_{ar} = \sqrt{\frac{c}{m_1 + m_2}} \tag{2.15}$$

$$\omega_r = \sqrt{\frac{c}{m_2}} \tag{2.16}$$

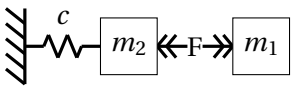

Figure 2.8: Flexible frame IPM

When the feedback refers to the position of the end-effector with respect to the fixed world ($y = x_1$), the obtained transfer function is of type D. The same parameter for the mass applies as in the type AR from equation 2.14.

2.2 Port-based modelling

According to [4], physical system interconnections are well-defined if the power flows are specified. In a physical system, input and output are related in the sense that their product has to give *power* as a result and, in this context, they cannot be considered and treated independently . A dynamical system can be interpreted as an object that elaborates an information flow received as an input and provides another information flow as an output depending on the input and the initial conditions [4]. Input and output can be considered together, as the system interface with the environment, which is referred to as a *power port*.

2.2.1 Bond graph basics

Port-based modelling is a domain-independent, energy-based method. In this sense, any physical system can be modeled by properly interconnecting the power ports of simple elements, each of which are characterized by certain energetic behaviors (storage, dissipation, conversion, etc.). A common characteristic of these simple elements is the fact that they have a port with a pair of external variables (*flows* and *efforts*). This duality provides the power exchange with the environment. The notion of *flows* and *efforts* consists of abstractions that allow a unified description throughout the different energetic domains. In the mechanical domain, the speed informations are called *flows* and the force informations are referred to as *efforts*.

Bond graphs are a graphical language for modelling physical systems using the port-based approach. In bond graphs, the idea is to interconnect each subsystem with an energetic bond that represents the power exchange. Figure shows an example of a bond graph, where two systems A and B are interconnected. The edge is the power bond, while e and f represent the effort and flow power ports, respectively.

The most important characteristics about bond graphs are [4]:

1. Each bond represents a port interconnection that contains both an effort and a flow.
2. The *half-arrow* does not indicate neither the positive direction of the effort nor the flow, but only the positive direction of the power.
3. The *causal stroke* (line at one of the edges of the interconnection) indicates the positive direction of the effort.

As mentioned before, bond graphs consist of simple elements with different energetic behaviors, which are:

1. *Storage elements:* can be classified on the basis of what kind of input signal they receive:

   (a) **C elements**: receive a flow as input and provide an effort as output;
   (b) **I elements**: receive an effort as input and provide a flow as output.

2. *Dissipation elements:* model the irreversible phenomena of the conversion of energy to the thermal domain. They are represented with the symbol **R**.

3. *Transformation elements:* are two-port elements whose characteristic is the power conservation. There is basically two types:

   (a) **Transformer**: represents a transformation in which a flow is mapped into another flow and correspondingly an effort into another effort. Represented by the symbol *TF* or *MTF* when modulated. Examples are gearboxes or electrical transformers.
   (b) **Gyrator**: represents a transformation in which a flow is mapped into an effort and an effort is mapped into a flow. Represented by the symbol *GY* or *MGY* when modulated. Typical example is a DC motor.

4. *Source elements:* are capable of generating energy. There are two kinds: source of effort (S_e) and source of flow (S_f).

Once a dynamical system is represented as a bond graph, it is possible to generate a set of mixed algebraic and differential equations, and from this is it possible to go to a state-space representation or a transfer function, as desired. In both these cases, the order of the system will be directly related with the number of storage elements with preferred integral causality.

If more background information is desired about bond-graphs, the reader is advised to take a look at [5].

2.3 Motion Controllers

In literature the 2 DOF (degrees of freedom) controllers are well known [3]. The label 2 DOF refers to the fact that there are at most two independent parts in the control signal u, namely a part independent of the measured output y and a variable dependent of the measured output y [6]. Even though it seems from the number of components R, F and C, that there might be three degrees-of-freedom, the fact is that given a compensator C there could be combinations of R and F that yield the same output y. This is why, according to [3], it is best to refer to this type of control systems as 3-CC (three control components). Figure 4.1 shows a 3-CC control system.

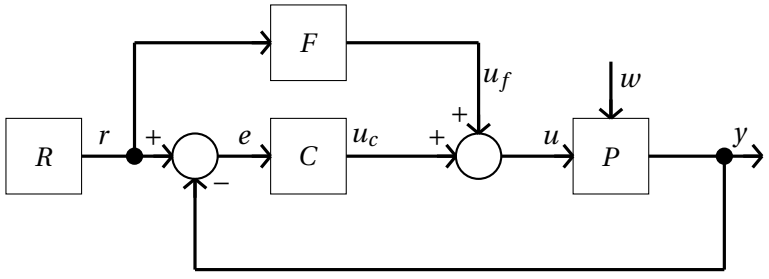

Figure 2.9: General 2 DOF or 3-CC servo system.

The main components are defined as [3]:

1. *Reference path generator R*: will indicate an approximation of the desired motion for the end effector. The signal should be chosen in harmony with the other components of the control system and the electromechanical plant.

2. *Feedback component C*: it is perhaps the most important component, because sometimes only with the reference R and the feedback component, a robust motion for the

system can be achieved. This is however, not always possible or desirable as it is difficult to design a component that can meet all the objectives. In a stable closed loop system, the output y has to follow the reference R with a small error e and has to cope with disturbances w in spite of model uncertainties. This can theoretically be achieved by a feedback component with a large gain, nonetheless, this can make the system unstable and implicates large power requirements and low measurement noise.

3. *Feedforward component F*: has the main objective of generating the forcing function u_f, which results in nominal tracking. Apart from that, its addition may improve the controller's performance without affecting the stability disturbance attenuation and robustness properties. Similarly to the feedback component, some considerations have to be made to avoid undesired behavior such as avoiding large or fast changing inputs.

4. *Plant P*: is the preexisting system that does not (without the aid of a controller or a compensator) meet the given specifications. It combines the actuator and the process, and expressed as a transfer function it gives the relation between input and output without feedback.

In the following subsections, the two different approaches for feedback components used in the present work, will be briefly explained.

2.3.1 PID algorithms

A PID has three parameters corresponding to the *proportional, integral* and *derivative* actions. In general, each of these actions has a specific function in motion control: the proportional action provides the desired bandwidth, the derivative action ensures stability and the integral action provides extra gain at the lowest frequencies so that low frequency disturbances can be suppressed.

The typical types of PID algorithms are:

1. Parallel PID
2. Series or interacting PID
3. Ideal or non-interacting PID

2.3.1.1 Parallel PID algorithm

In this type of controller the gains K_p, K_i and K_d are contributing to the controller output u_c independently from each other, as it can be seen in the structure of Figure 2.10.

This algorithm is simple to understand, but the tuning procedure is not that intuitive. The reason is that each of the terms act on a fresh, unadulterated error term, and then the results are added at the end. This implies that when changing one of the gains, the others should be adjusted at the same time as well, in order to preserve the current behavior. The output of the controller is given by:

$$C(t) = K_p e + K_d \dot{e} + K_i \int e \tag{2.17}$$

Because of all the possible combinations that such construction can render, there exists a large quantity of tuning approaches. In the present work, a pragmatic way will be used.

2.3.1.2 Series PID algorithm

The series algorithm is the classical and oldest PID structure. In it, the output of the P-action goes into the I-action and then to the D-action. This means that by changing the P-action the

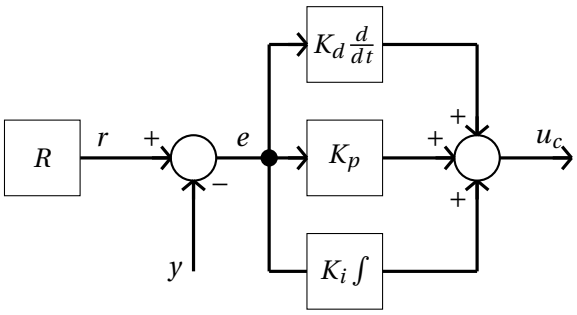

Figure 2.10: Parallel PID structure.

other two are affected, or if adjustments are made to the integral action, they will also reflect on the derivative one. This can be observed in Figure 2.11.

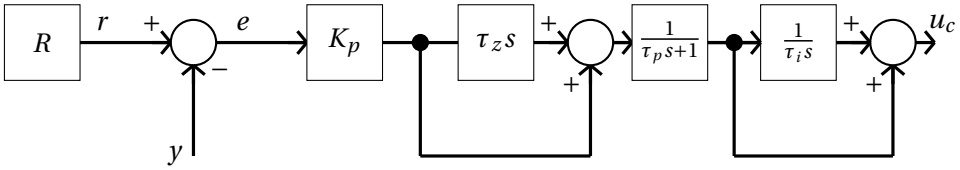

Figure 2.11: Series PID structure (with derivative filter).

The transfer function for the series algorithm is given by:

$$C(s) = K_p \cdot \frac{s\tau_z + 1}{s\tau_p + 1} \cdot \frac{s\tau_i + 1}{s\tau_i} \tag{2.18}$$

In equation 4.34, the τ_z represents the time period $(1/\omega_z)$ at which the damping action begins, the τ_p is the time period $(1/\omega_p)$ at which the damping action finishes, and the τ_i $(1/\omega_i)$ indicates the end of the integral action.

Because of the interaction between the terms, rules of thumb have been developed in order to facilitate the tuning of this type of algorithm. These rules help determine the gain K_p, and the values for τ_z, τ_p and τ_i. The recommended value for β is 10 because it represents the ratio between ω_p $(1/\tau_p)$ and ω_z $(1/\tau_z)$, where their values should satisfy that $\omega_z \leq 3\omega_c$ and $\omega_p \geq 3\omega_c$.

$$K_p = \frac{\omega_c^2 I_{total}}{\sqrt{\beta}} \tag{2.19}$$

$$\tau_z = \sqrt{\beta}\frac{1}{\omega_c} \tag{2.20}$$

$$\tau_p = \frac{1}{\sqrt{\beta}\omega_c} \tag{2.21}$$

$$\tau_i \geq \sqrt{\beta}\frac{2}{\omega_c} \tag{2.22}$$

2.3.1.3 Ideal PID algorithm

In this algorithm the only interaction is that the P-action also scales the effect of the I-action and D-action. This can be seen in Figure 2.12

The transfer function for the ideal PID algorithm is given by:

$$C(s) = K_p\left(1 + \frac{1}{T_I s} + T_D s\right) \tag{2.23}$$

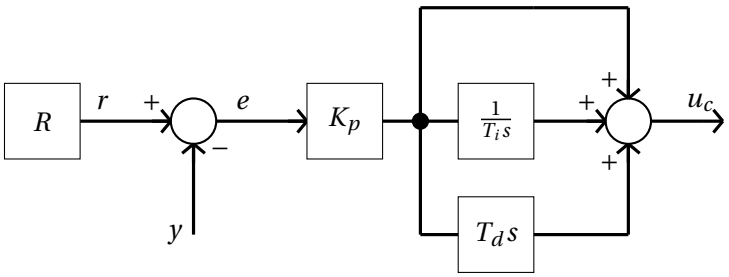

Figure 2.12: Ideal PID structure.

2.4 Controlled Passive Actuation (CPA)

The concept of *passive dynamic walking* was introduced in the late 1980's by Tad McGeer [7]. These passive dynamic walkers were able to walk stably down a small decline without the use of any actuators. According to [8], these machines provide an excellent example of how good machine design can yield stable and energy efficient walking mechanisms. These ideas, however, are only being implemented recently in the fully actuated version of walking robots that are designed and controlled.

A walking device operating passive dynamically can be efficient because it needs no energy for stabilization or control, only power to recover small losses [9]. The most fundamental cause of this energetic loss is impact, primarily between the feet and ground. In a sense, the passive-dynamic approach is the opposite of the trajectory control approach, which tends to constantly control actuation to force a system against its natural dynamic tendencies[9]. Nevertheless, to bridge the gap between passive and active walkers, research has been made into the implications of adding small number of actuators to otherwise passive systems. The two major advantages of this combination are that, first, actuating a few degrees of freedom on a passive system can provide the best possible combination between energy efficiency and the robustness of actively controlled systems. A second advantage is that, by allowing the dynamics of the system to solve, for the most part, the control problem, it may be possible to simplify the control problem that is solved by the actuators [8]. This combination of active and passive systems is referred to as *Controlled Passive Actuation*. In general, it aims at reducing the energy flow through electric actuators by actuating with a combination of an energy storage element and a Continuously Variable Transmission [10].

2.5 Dual-Hemi CVT

This section describes the construction of the Dual-Hemi CVT, which stands for a continuous variable transmission. The system consists of two hemispherical friction wheels that transmit power and facilitate the alternating of the transmission ratio. The design was specifically thought for the use along with control passive actuation (CPA).

2.5.1 Mechanical Design

The design, documented in [1], consists of two hemispherical friction wheels which have the ability to alternate their contact angle. In order to make this alternation possible, the system makes use of two separate frames, one of which is fixed and the other can be repositioned according to the desired transmission ratio. Each frame holds one of the friction wheels in place. The mechanism that takes care of the positioning of the adjustable friction wheel frame is independent from the mechanical path of the power transmission. Thus, the Dual-Hemi CVT can be analyzed as two separate mechanisms: the *power transmission mechanism* and the *reconfiguration mechanism*. Both of them are shown in Figure 2.13 and will be described in more detail next.

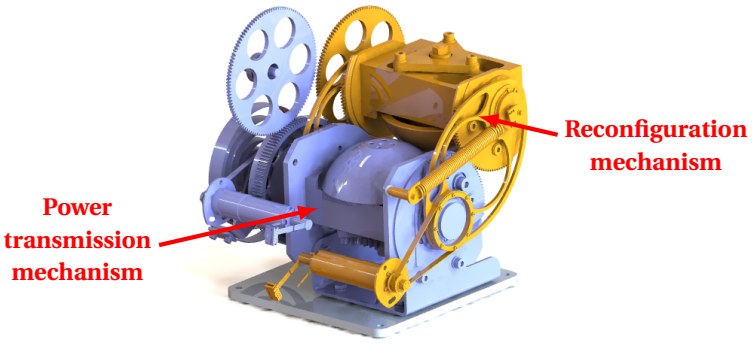

Figure 2.13: The two mechanisms of the Dual-Hemi CVT

2.5.1.1 Power transmission mechanism

In the system the power split principle is also applied, using a planetary gear to transmit part of the power through the continuous variable transmission, and the rest through a straight mechanical path.

For the power transmission design, two important couplings have to be made. The ring wheel of the planetary gearbox was coupled to the fixed friction wheel (see green part of Figure 2.14), and the adjustable friction wheel was connected to the carrier of the planetary gear (see red part of Figure 2.14). Both connection are made using sets of crown gears. The parts involved in the power transmission mechanism can be seen in Figure 2.14.

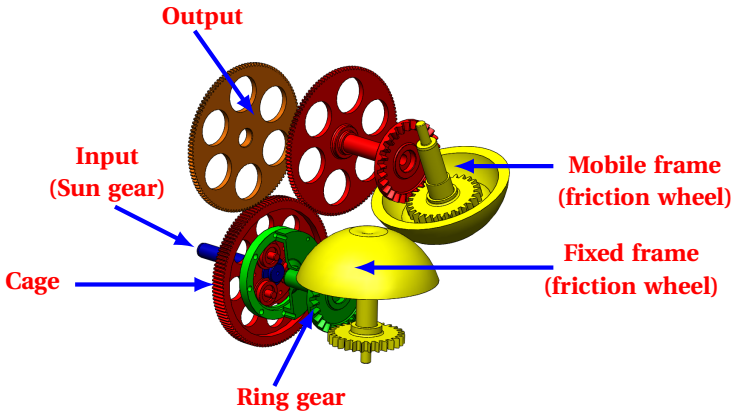

Figure 2.14: Power transmission path of the Dual-Hemi CVT

For spring driven actuation, the sun gear is connected to a clock spring and the output coupled to the carrier of the planetary gear.

2.5.1.2 Reconfiguration Mechanism

The reconfiguration mechanism is composed by the mobile frame, a gravity compensator (spring) and a DC-motor. The movement of the mobile frame is guided with a rail, which provides proper orientation and alignment. Apart from the guiding, and to ensure that the frames can withstand the contact force between the friction wheels, the design uses two "flexible arms" [1]. The DC-motor that actuates the friction wheels structure is connected with a timing belt to one of the guiding arms. Furthermore, to reduce the required actuation force of the motor, a gravity compensator in the form of spring is used.

Figure 2.15 depicts the main components the reconfiguration mechanism.

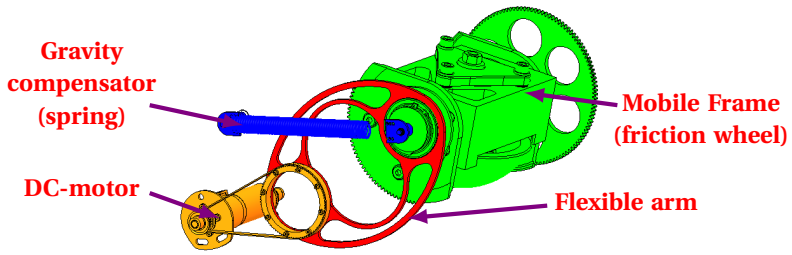

Figure 2.15: Parts of the reconfiguration mechanism of the Dual-Hemi CVT

3 Modelling

This chapter describes the steps followed to reach competent models for the two main mechanisms that form the Dual-Hemi CVT, with focus on the reconfiguration system, which is the one in charge of the change of the transmission ratio.

3.1 Modelling of the DH-CVT Spring CPA to Load Path

As explained in section 2.5, the Dual-Hemi CVT is divided in two principal mechanisms. This part of the report explains the modeling process for the mechanism in charge of the transmission of the power from the spring driven by an electric actuator (input), to the load of our system (output).

3.1.1 Derivation of IPM of the DH-CVT

From a visual analysis of the transmission and the 3D CAD models we obtained the ideal physical model (IPM) shown in Fig. 3.1. An ideal physical model is a way of representing our system graphically, where the masses have a constant value, a line between two elements can be considered as an infinetly rigid connection, the springs are elements without mass and the transmissions are considered to have 100% efficiency.

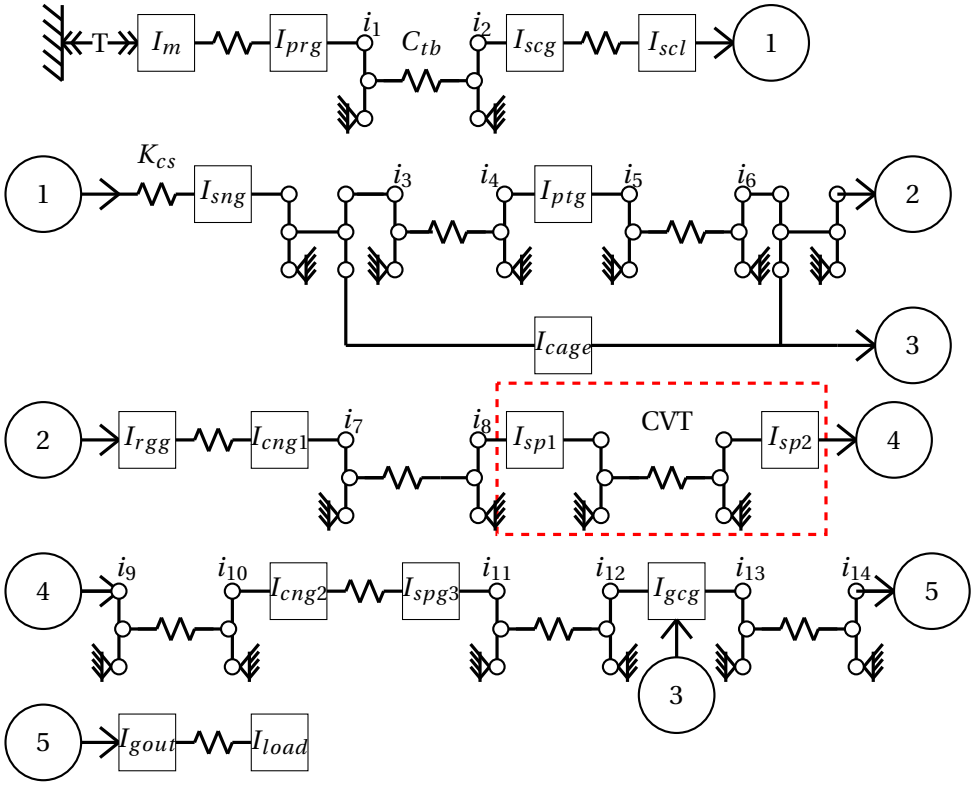

Figure 3.1: IPM of PS-CVT Mechanism. A list with the values for each element can be find in Appendix A.1

In Fig. 3.1 we can observe a source of torque at the input (motor) and a considerable number of inertias connected via springs (stiffnesses). In the diagram, all the stiffnesses that are missing a label are either the rotational stiffnesses of the shafts and bars, or the stiffnesses between the teeth of the gears. Since they have very high values from the beginning, not much attention is

paid to them, as later they will be considered as rigid connections.

The inertias were obtained with help of the CAD model for the Dual-Hemi CVT, since it contains the dimensions and materials for each element of the mechanism. The stiffness of shafts was calculated using the following equation:

$$K_{st} = \frac{\pi G d_{st}^4}{32 L_{st}} \tag{3.1}$$

Where K_{st} is the rotational stifness of the shaft, G is the shear modulus of the material, d_{st} is the diameter of the shaft, and L_{st} is the length of the shaft [11].

The clock spring stiffness was calculated using the following equation:

$$K_{sg} = \frac{E_{sg} w_{sg} t_{sg}^3}{12 L_{sg}} \tag{3.2}$$

Where K_{sg} is the rotational stiffness of the spring, E_{sg} is the Young modulus of the material, w_{sg} is the width of the spring, t_{sg} is the thickness of the spring, and L_{sg} is the length of the spring. The length can be calculated as follows.

$$L_{sg} = \frac{\pi n_{sg}(D_{sg} + d_{sg})}{2} \tag{3.3}$$

Where n_{sg} is the number of spirals in the spring, D_{sg} is the diameter of the outer spiral and d_{sg} is the diameter of the inner spiral of the spring[11].

The values for the stiffness between the teeth of the gears are consider as infinite, since they are made of very stiff materials, and the system will not be subjected to very high loads and/or input forces.

3.1.2 Model reduction and conversion to Bond Graph

In order to reduce the model from Fig. 3.1 an intuitive method was applied as described in [12]. The first step to apply this reduction, is the elimination of all the transmissions. In this way, we can check the relative importance of each element, since the transmission ratios can reduce or magnify the effect that each of them has in the global system.

Once that the transmissions have been removed from the IPM (see Fig. 3.2), we can proceed with the model reduction. The following step consists in leaving out the elements according to one of the criteria mentioned in subsection 2.1.1. In our case the criterion number 1 was applied, because the calculation of the rotational stiffness of the shafts and bars and the stiffness between the teeth of the gears resulted in very high values.

In Fig. 3.2 it can be seen that most of the stiffness in our model can be consider as infinite, and thus we can combine the inertias that are connected rigidly. In the diagram the inertias that can be combined in one element are enclosed on boxes, where each color represents one resultant inertia element.

The resulting diagram after removing the elements of the system that are not relevant in the dynamics of the system is shown in Fig. 3.3. Here we can see more clearly how the Dual-Hemi CVT works. One of the possible energy flows can be described as follows: the input of the system is a torque (T) generated by the electric actuator (motor), which has an inertia I_m and

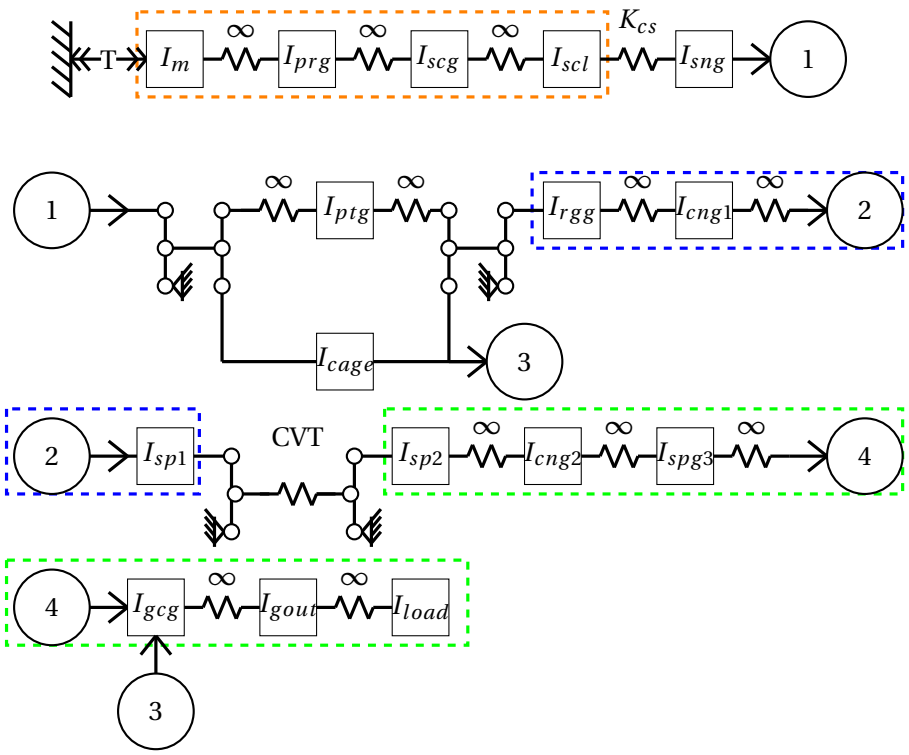

Figure 3.2: IPM of PS-CVT Mechanism without transmissions.

then this energy goes into the spring K_{cs} used for the Controlled Passive Actuation. Then the energy in the spring is transmitted to the sun gear I_{sg} of the planetary gear, which transmit the power to the planet gears I_{ptg}. From this point the power can be splitted, being transmitted to the ring gear I_{rgg}, or to the cage that holds the planet gears I_{cage}. When power flows through the ring gear I_{rgg} it is transmitted by means of the CVT formed by the two semi-spheres, and when it goes through the cage of the planets the power is transmitted directly into the load I_{load}, a more detailed explanation is given in [13].

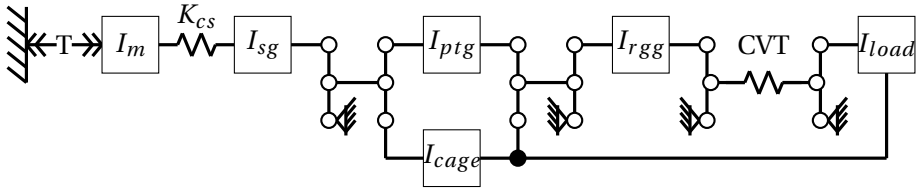

Figure 3.3: Reduced IPM of PS-CVT Mechanism

From the IPM model in Fig. 3.3, a transformation to the Bond Graph [14] (port based modeling) representation was made, trying to get more insight from the system, since this type of model gives information about the direction of the flow of energy (signs), the dependency of the elements with each other (causality) and gives us the possibility to analyze the flow of energy between different domains (electrical and mechanical in our case). Besides, there are established methods to analyze the dynamics of the system without loss of information [5]. The outcome of the transformation to a Bond Graph can be seen in the Fig. 3.4, where the elements that form the electrical domain of the motor (T) were added, then we use a source of flow Sf (current) as an input, because the motor is controlled by means of current. The elements I_e and R_e represent the inductance and electrical resistance of the motor, respectively, the gyrator GY represents the motor constant.

In the Bond Graph we can also see that the velocity of several inertias is dependent on the rest, due to the fact that we are considering and infinite stiff connection between the elements.

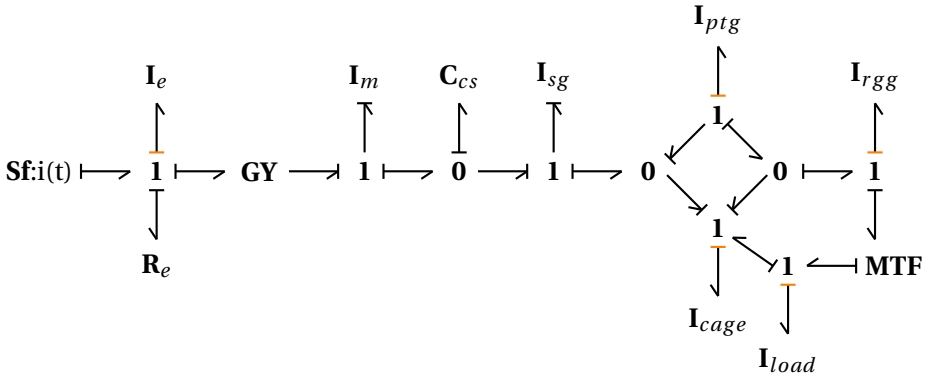

Figure 3.4: Bond graph from the reduced IPM of the PS-CVT

3.1.3 Model Verification

Once that the Bond Graph was obtained and checked, some simulations were carried out in order to see if the behavior of the model was the expected.

If we compare the governing kinematic equation for a planetary configuration, equation 3.4, with the results of our model simulation it is possible know how competent our model is [15].

$$\omega_{E1} = k_1\omega_{E2} + k_2\omega_{E3} ... + k_N\omega_{E(N+1)} \tag{3.4}$$

In equation 3.4, ω_{E1} represents the angular velocity of a given component $E1$ while $\omega_{E2}, \omega_{E3}, ..., \omega_{E(N+1)}$ represent the angular velocities of the N independent controlled components, and $k_1, k_2, ..., k_N$ the transformation ratios dependent on the geometry of the gears.

In the Dual-Hemi CVT, one of the key parts of the mechanism is the simple planetary gear with a single carrier, sun gear and ring gear. Even when the gears can be connected in six different ways, not all the scenarios need to be analyzed to develop a governing kinematic equation. If we let the sun and ring gear be the drive inputs, and the carrier (cage) as the drive output. Then we have:

$$\omega_{cage} = k_1\omega_{sg} + k_2\omega_{rgg} \tag{3.5}$$

If we assume $\omega_{rgg} = 0$ then from equation 3.5 we can get the ratio k_1:

$$k_1 = \frac{\omega_{cage}}{\omega_{sg}} \tag{3.6}$$

Nevertheless since all the transmissions were already eliminated during the model reduction, our $k_1, k_2, .., k_N$ should be equal to one. Thus if we consider as initial condition that the load is at rest (it is connected to the carrier or cage) $\omega_{cage} = 0$ then, from equation 3.5 , the velocities of the sun and ring gear become:

$$\omega_{rgg} = -\omega_{sg} \tag{3.7}$$

To verify this model, an experiment was designed. As input, the CPA was fed with a constant torque and had, for the first five seconds, a transmission ratio = 0. During the experiment we aimed to see the following behaviors:

1. A difference between the motor speed ω_{motor} and the sun gear speed ω_{sun}, due to the delay caused by the compliance of the spring at the input.
2. The velocity of the ring gear ω_{ring} to be opposite from the velocity of the sun gear ω_{sun}.
3. The velocity of the output ω_{load} should be zero, while the transmission ratio is equal to zero.

The results of the simulation for the experiment are shown in Fig. 3.5. A wavelike behavior in the curves is observed, this is due to the compliance of the spring located at the input of the system. It is possible to observe, that all the expected behaviors are present.

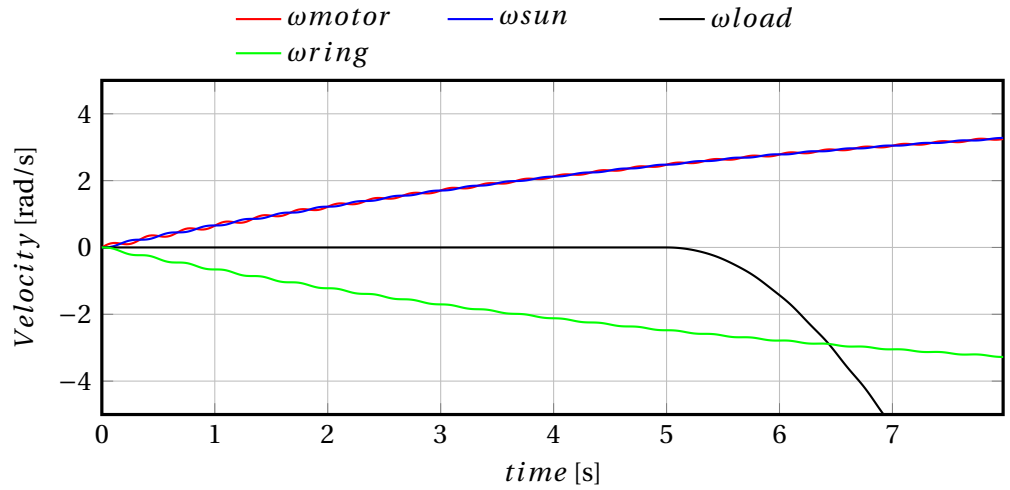

Figure 3.5: Angular velocities in elements of CVT

Furthermore, it is important to look at the behavior of the system, more specifically, when the transmission ratio is changed. Because of this, in the same experiment mentioned above, after the first five seconds the transmission ratio is modified with a ramp signal. By doing this, we expect the angular velocity of the load to be different than zero and to increase in the opposite direction of the ramp.

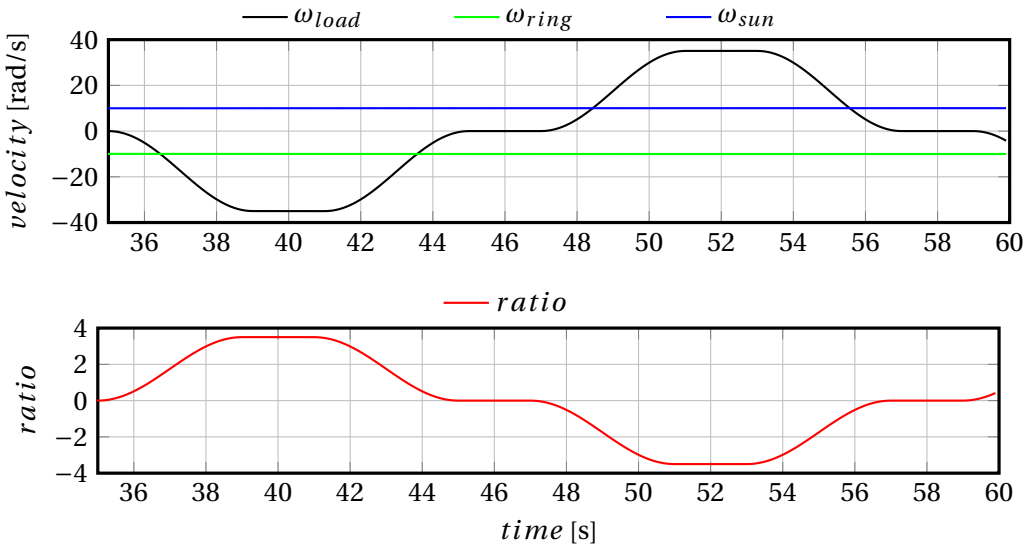

Figure 3.6: Variation of transmission ratio and comparison of the ω_{rgg} and ω_{load}.

In Fig. 3.6 the change in the transmission ratio in the CVT (MTF) is shown. We can see how, at the moment that the transmission ratio is different from zero, the angular velocity from the ring gear ω_{rgg} starts to be transmitted to the cage, which is rigidly connected to the load with the expected relation, in equation 3.8, since the all the energy is in the ring gear before the power start to flow to the load.

$$\omega_{load} = i_{CVT}\omega_{rgg} \tag{3.8}$$

Since the two key points of the model have a satisfactory behavior, we can conclude that our model is kinematically correct enough to understand the dynamics of the Dual-Hemi CVT, at least in the part of the system that takes care of the power transmission from the input (torque in the spring) to the output (motion of the load). No further investigation for this part of the system will be done in this phase of the project, due to the lack of sensors to know the position of each element. Nevertheless, this model can be verified using the setup in future work, to be used for the improvement of the controller for this part of the DH-CVT. The reconfiguration mechanism model will be studied in the next section (3.2).

3.2 Modelling of reconfiguration mechanism

In this section the process to develop the model for the reconfiguration system will be described. This model is of higher importance for the present work, since this mechanism limits the bandwidth of the Dual-Hemi CVT [2]; and, in addition to this, the torque and position control in the load depends heavily on the transmission ratio.

The same procedure presented in section 3.1 is followed to develop the model of the reconfiguration mechanism.

3.2.1 IPM from mechanism and calculations

To start the modeling of the reconfiguration mechanism, the same approach, as for the power transmission part, was used. First a visual analysis of the actual setup and the 3D CAD models was done, from where the ideal physical model (IPM) shown in Fig. 3.7 was obtained.

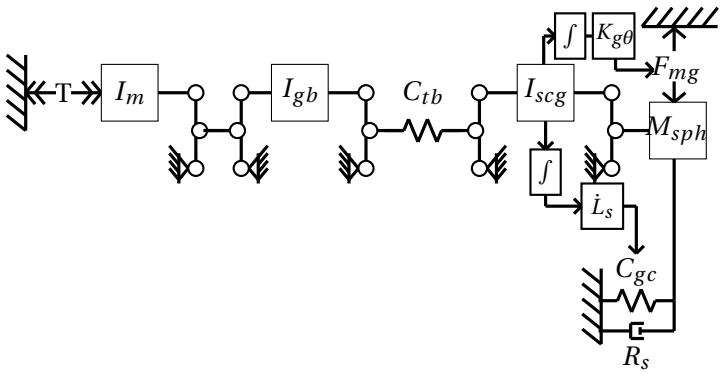

Figure 3.7: IPM of Reconfiguration Mechanism

From the insight obtained in section 3.1.2, the stiffnesses of the shafts and bars were considered as infinite. Moreover, the groups of inertias rigidly connected have been added into one element. Because of this, the model already takes into account these reductions. In it we can see a source of torque T (Motor), with its inertia I_m, then we can see a transmission (gearbox) with the inertia I_{gb} at the output shaft, then there is a belt drive transformer with the linear stiffness C_{tb} for the timing belt, the inertia of the secondary gear I_{scg} drives the mobile arm (considered as a lever) with the load M_{sph} (mass of sphere module) connected at the other end. In the load mass we have the gravitational force F_{mg}, the gravity compensator C_{gc} and

some rolling friction forces R_s.

Just like in the model for the power trasnmission part of the CVT, the inertias were obtained from the CAD model of the reconfiguration mechanism. The stiffnes of the timing belt was obtained from the manufacturer catalog [16], the linear stiffness of the gravity compensator is known (1800 N/m)and the rolling friction was calculated according to [1] as follows:

$$F_{rol} = \mu_{rol} F_N = 3.2 \tag{3.9}$$

Where F_{rol} is the rolling friction force, μ_{rol} is the frictional rolling coefficient (0.002) and F_N is the normal force (1600 N), in this case is the force required to press the spheres against each other and transmit the required torque without slip in the contact area. We can say that the friction required to transmit the power affects also the performance of the reconfiguration mechanism. The value of each element can be seen in the Appendix B.1.

In this case, no further reduction was made to the IPM. One reason is that the model is already relatively simple, and another is that we are interested in understanding the dynamics of the mechanism as much as possible. The aim of this model is to develop a function that describes the non-ideal behaviors of the mechanism, like the friction and residual forces that are in the system and have not been identified.

3.2.2 Conversion to Bond Graph

Given the fact that a bond graph model gives more insight on the energy flow direction and the dependencies of elements, a conversion from the IPM to this representation was made. Since this model representation is domain independent, the elements that form the electrical domain of the motor were added to analyze their contribution to the dynamics of the system, Fig 3.8 shows the resulting Bond Graph.

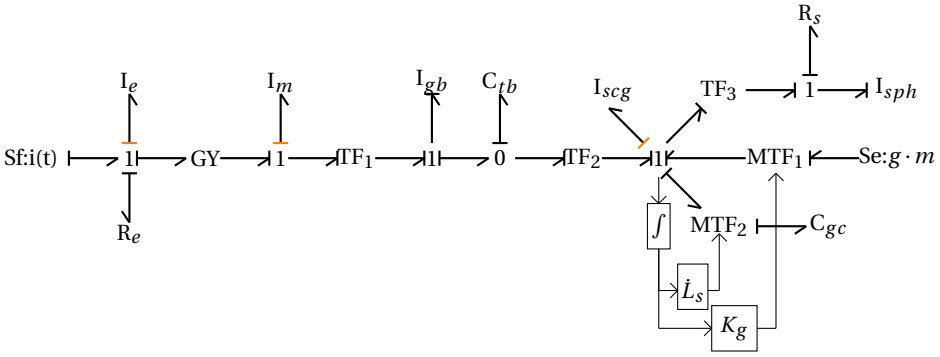

Figure 3.8: Bond graph from the IPM of the reconfiguration mechanism

In the figure, the gyroscope GY represents the motor constant, the first transformer TF_1 is the transmission ratio of the gearbox, the second transformer TF_2 is the transmission ratio in the belt drive transmission, TF_3 represents the length of the lever (mobile arm). MTF_1 and MTF_2 are considered as modulated transformers because the gravitational is dependent on the angle, as depicted in equation 3.10 and spring forces are affected by change in the length of the gravity compensator. A source of flow Sf is used as input, because the current control is applied to the motor. The source of effort Se represents the gravitational force acting on the mobile sphere module.

3.2.2.1 Determining transformations and the initial conditions

In this section, the derivation of the ratio, for the modulated transformer, that controls the change in the state of the gravity compensator is done. Moreover, the initial conditions in the configuration of the mechanism are studied, since spring and gravitational forces are position dependent.
Having the structure of the Bond Graph, we proceed to establish the initial conditions of the system. For this, an observation to the geometrical configuration of the mechanism is needed.

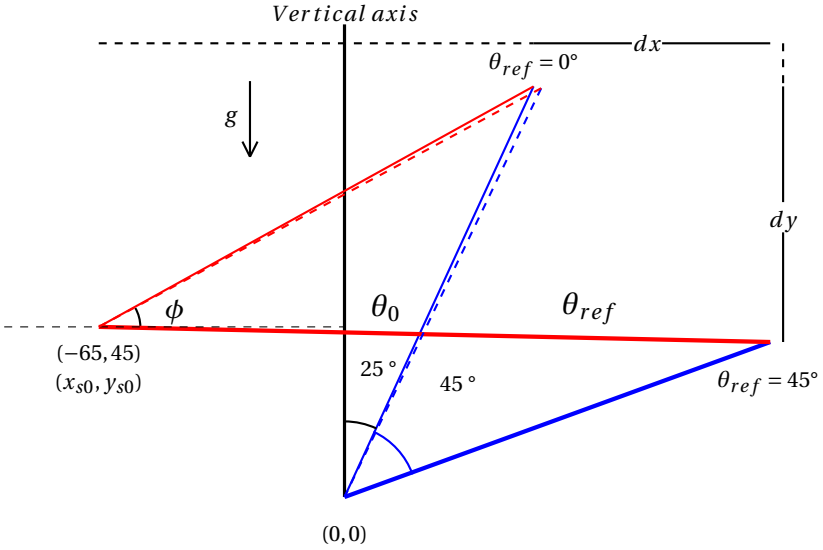

Figure 3.9: Geometrical configurations of spring and lever. The red lines represent the spring length (variable) and the blue lines the lever length (fixed). The dashed lines are in the position for the spring initial condition. The solid lines represent the limits of position reached by the mechanism.

In Fig 3.9 we can see how the reconfiguration mechanism looks like an inverted pendulum. Thus in the model we need to measure the angle with respect to two references. First with respect to the vertical axis, referred to as θ_0, in order to know the torque generated due to gravity that can be expressed as:

$$\tau_g = L_l \cos(\theta_0) m_{sph} g \tag{3.10}$$

In Equation 3.10 τ_g is the torque generated due to gravitational forces, L_l is the length of the flexible arm (lever), m_{sph} is the mass of the sphere and g is the acceleration due to gravity ($-9.81 m/s^2$). This equation represents the gain K_g which is fed into MTF_1 from the Bond Graph in Figure 3.8. The angle θ_{ref} (angle of the reconfiguration mechanism), will be measured with respect to the first solid line ($\theta_{ref} = 0$ in the figure), since this is the end stop in the mechanism, i.e. is the position when we ask the lever to go to a zero angle position, then it can be say that $\theta_0 = \theta_{ref} + 25°$. This θ_{ref} is the required feedback for the controller.

From Fig 3.9, the spring's longitude can be found using an imaginary right triangle, where the catheti are dx and dy, and the hypotenuse is the length of the spring (L_s) itself . The magnitude for the catheti is given by:

$$dx = L_l \sin(\theta_0) - x_{s0} \tag{3.11}$$

$$dy = L_l \cos(\theta_0) - y_{s0} \tag{3.12}$$

In Equations 3.11 and 3.12, x_{s0} and y_{s0} represent the coordinates of the spring's pivot (fixed point).

From the above model we can infer that, for the upright position (with respect to $vertical\ axis$ from Figure 3.9), the following equation, where L_s represents the spring length, can be obtained using Pythagoras Theorem:

$$L_s = \sqrt{dx^2 + dy^2} \tag{3.13}$$

From now, and given the IPM representation drawn earlier it is possible to foresee the bond graph model, having a generalized representation like the one shown in Fig 3.10.

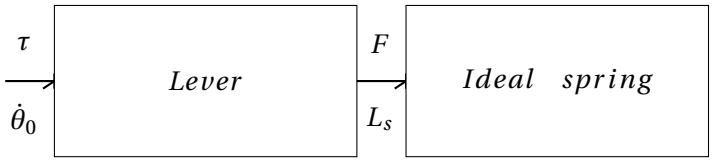

Figure 3.10: Bond Graph for lever-spring mechanism.

The kinematic relation $L_s = L_s(\theta_0)$ can be described as a transformation between coordinates (angular to translational). Therefore the description of the mechanism includes modulated transformer (MTF_2). In order to obtain this transformation relation for MTF_2, the Jacobian is found by differentiating the term with respect to θ_0, i.e. the respective velocity $\dot{L}_s$. Substituting values of dx and dy from Equations 3.11 and 3.12 into Equation 3.13 and taking the derivative of the result, yields:

$$\frac{\partial L_s}{\partial \theta_0} = \frac{2L_l\cos(\theta_0)(L_l\sin(\theta_0) - x_{s0}) - 2L_l\sin(\theta_0)(L_l\cos(\theta_0) - y_{s0})}{2\sqrt{(L_l\cos(\theta_0) - y_{s0})^2 + (L_l\sin(\theta_0) - x_{s0})^2}} \tag{3.14}$$

Representing the above equation in matrix form, where this transformation relation (matrix) is referred to as the Jacobian (J), we have:

$$\dot{L}_s = \left[\frac{2L_l\cos(\theta_0)(L_l\sin(\theta_0) - x_{s0}) - 2L_l\sin(\theta_0)(L_l\cos(\theta_0) - y_{s0})}{2\sqrt{(L_l\cos(\theta_0) - y_{s0})^2 + (L_l\sin(\theta_0) - x_{s0})^2}}\right]\dot{\theta}_0 \tag{3.15}$$

Since the modulated transformer is power continuous element, the constraint $P_{in} = P_{out}$ (Power at input equals power at output) applies, meaning that:

$$P_{in} = \tau^T\dot{\theta} = P_{out} = F^T\dot{L}_s \tag{3.16}$$

From substituting Equation 3.15 (using J as representation for the Jacobian matrix) in 3.16, we get:

$$\tau^T = F^T J \tag{3.17}$$

Transposing both sides of the equation leads to the relation of the torque to the force:

$$\tau = J^T F \tag{3.18}$$

With this equation we have achieved a generalized form to do coordinate transformation. Thus it can be concluded that the transmission ratio of the MTF_2 is described by the matrix found in equation 3.15. And the input to this transformer is the angular position, resulting from the integration of the velocity at the axis of rotation of the lever, as shown in Fig 3.8. For this integration the initial conditions of the system are taken from the Fig 3.9 (dashed lines), where the spring length is $106mm$ and there is an angle of 5° with respect to the vertical axis.

3.3 Estimation of Torque generated by the effect of non idealities

After establishing the initial conditions (initial geometrical configurations) of the reconfiguration mechanism, and the calculation of transmission ratio for the modulated transformer, the developed model can be use as a tool to estimate the torques dependent on the friction and spring residual forces. The model created in Section 3.2.2 and shown in Figure 3.8, is formed by ideal elements. The assumptions made for the estimation of the torque generated due to non-idealities, is that the differences between the torque simulated for the ideal system and the torques generated in the setup is created to compensate the friction and residual forces. It is also assumed that the non idealities can be modeled as a single friction element acting on the axis of rotation of the flexible arm (lever). In subsection 3.3.1 the procedure follow for this estimation is described.

With the ideal model of the reconfiguration mechanism and the setup of the Dual-Hemi CVT, an experiment was designed, where the mechanism was moved along all the range of positions and with an increasing velocity. The aim of this experiment was to observe if the torque generated (with a provisional PID controller) to control the system was increasing proportionally with the velocity [17]. If this happens, it would mean that the system has viscous friction acting on it.

From the fact that the model has an ideal behavior, we can apply a reduction to the model from Fig 3.7 , keeping the most significant stiffness (C_{gc}) and eliminating all the transmissions, we end up with the system shown in Fig 3.11.

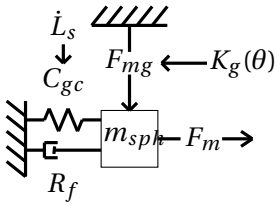

Figure 3.11: Reduced IPM of Reconfiguration Mechanism

From the system in Fig 3.11 the following equation that describes the dynamics of the system can be obtained. In the equation 3.11 F_m is the force generated due to the motor torque, R_f is the unknown friction in the system, which according to the discoveries made in [2], this friction has a position dependency; m_{sph} is the mass of the mobile sphere module, C_{gc} is the linear stiffness of the of the gravity compensator and x is the linear displacement of the mass.

$$F_m = m_{sph}\ddot{x} + R_f(\dot{x}, x) + C_{gc}x \tag{3.19}$$

In equation 3.19, we know the values of m_{sph} and C_{gc}, and in the experimental setup we can measure the position x of the load, thus, it is possible to know $\ddot{x}$ and $\dot{x}$, leaving as unknown only the term R_f. Which can be found rewriting 3.19 as follows.

$$Fm - m_{sph}\ddot{x} - C_{gc}x = R_f(\dot{x}, x) \tag{3.20}$$

From equation 3.20 it can be concluded that if experiments to explore the behavior of the system at different speeds, and moving the reconfiguration mechanism along all the operational range, then it is possible to estimate the torques generated due to friction. This will be demonstrated in 3.3.1.

3.3.1 Experiments and findings

As explained above, the experiments carried out during the modeling process have the aim to know the torques generated due to position and velocities dependent non-idealities in the system. The desired path was introduced in both the ideal model and the real setup, giving the following results.

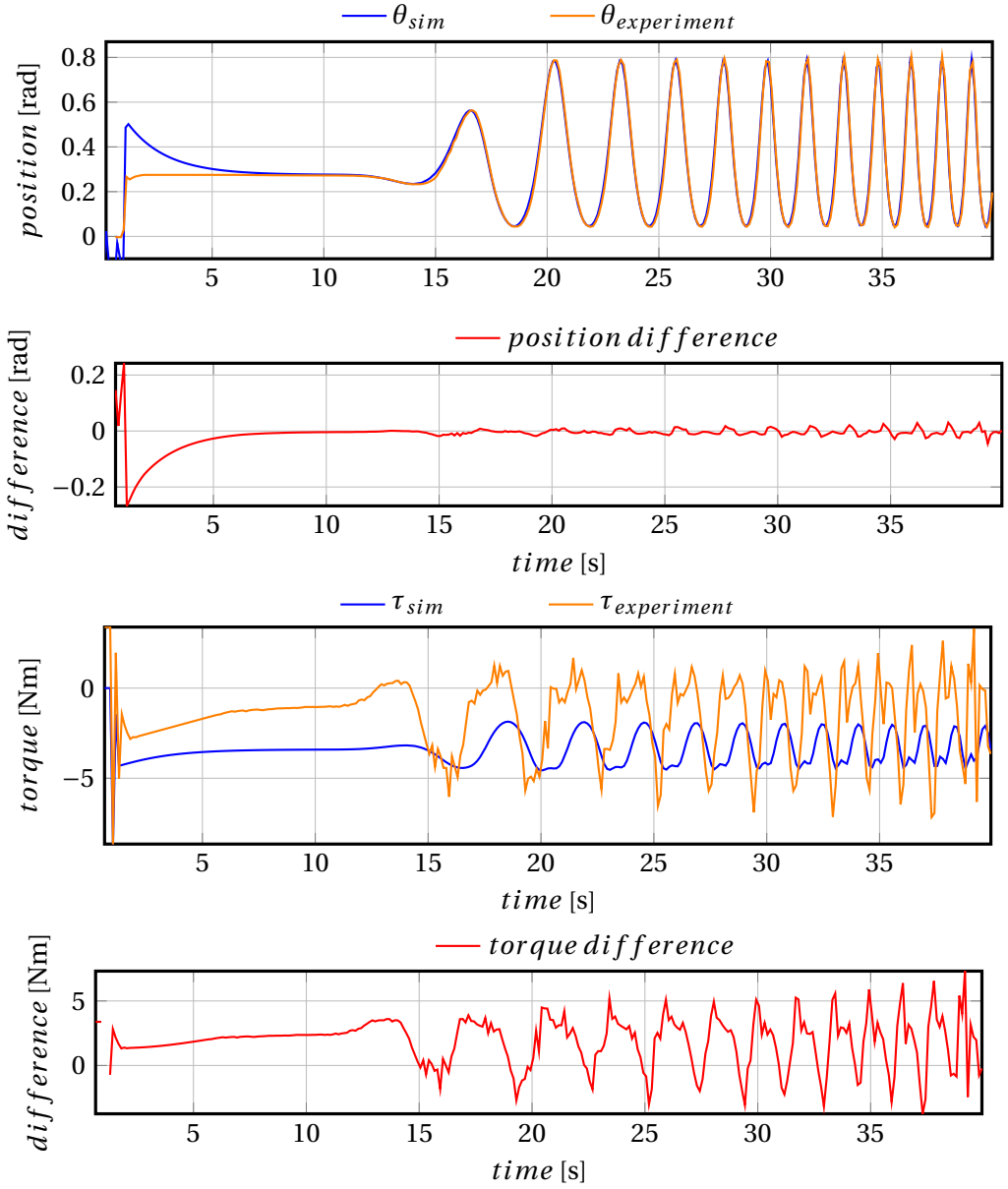

Figure 3.12: Comparison of position and torque in simulation of ideal system vs experimental results

In Fig 3.12, it can be seen how the tracking of the system behaves pretty much the same in simulation and in real experiment. From these experiments we found the difference in the torque generated, and then plot this residual torque versus the angular velocity and position, in order to have a friction model for our unknown element , which will handle all the torque generated due to non-idealities, as explained before.

A model for the velocity dependent friction and residual forces was obtained after applying a filter to the difference in torque, and then plotting the extra torques generated versus the velocity of the mobile module. The experimental results shown in Fig 3.13 (Left) resembles a

Stribeck friction model, as shown in [18], in the region where velocities are close to zero. A general description of friction is given by:

$$\tau = \left\{ \begin{array}{cc} \tau_\omega & if\ \omega \neq 0 \\ \tau_e & if\ \omega = 0\ and\ |\tau_e| < \tau_s \\ \tau_s sgn(\tau_e) & otherwise \end{array} \right\} \tag{3.21}$$

where τ is the torque generated due to friction in general (velocity dependent), τ_s is the torque generated from the stiction and τ_e is the torque resulting from external forces (spring residual forces). A very accurate model to describe the Stribeck friction effect is the LuGre model, which is presented in [19] and explained in detail in [20]. However, in the experimental results, the sign function $sgn(\tau_e)$ does not have a linear behavior due to the non ideal spring residual forces. Due to time constraints during the project, it was decided to create a continuous (polynomial) function that approximate the results. As it was faster than the identification of friction and residual forces individually. This friction-residual model has a non linear dependency on the velocity (viscous), together with coulomb friction and stiction due to the pressure of the spheres against each other.

In Fig 3.13 (Left), it can be observed that the friction model is shifted from zero. This corresponding to the experimental results, i.e. the difference of torques observe in Figure 3.12.

In order to obtain a model for the position dependent friction-residual torques, several experiments with different paths and velocities, were carried out. These experiments have the models shown in Fig 3.13 as outcome. Were the velocity dependent function results in a linear model and the position dependent torques are depicted by the function shown on the right Figure. The combination of the position and velocity dependent friction-residual models gives very good results when the change of ratio requires either low or high velocities from the reconfiguration mechanism.

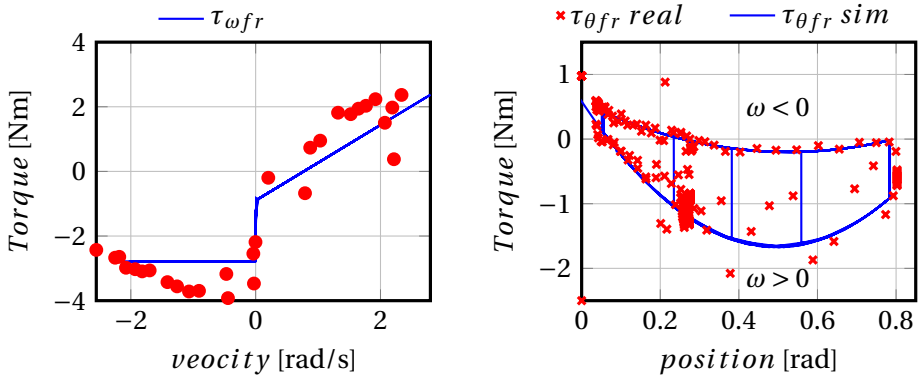

Figure 3.13: *Left* - Velocity dependent friction-residual torque. *Right* - Position dependent friction-residual torque.

In Fig 3.13 (Left), the friction dependent on the velocity shows viscous friction in one direction, while in the other there is only coulomb friction. In Fig 3.13 (Right), we can observe an hysteresis effect in the reconfiguration mechanism. This hysteresis is dependent on the acceleration of the movements done by the mobile module. In [2] it has been already explained, as the maximum torque that can be applied to the reconfiguration system varies depending on the direction of the movement. This is shown in Figure 3.14.

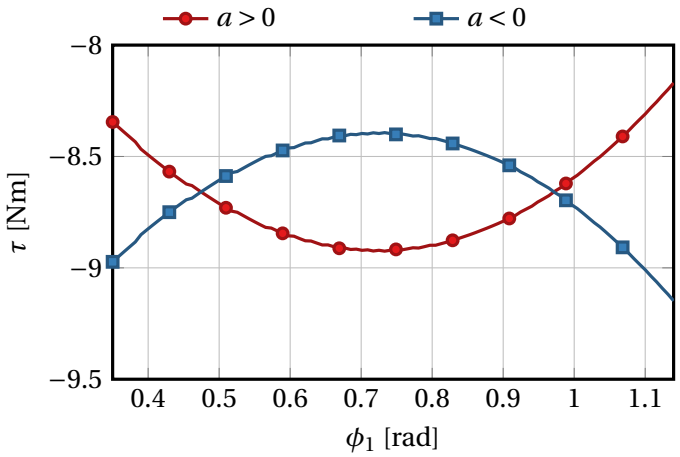

Figure 3.14: Max magnitude of the torque that can be applied to the reconfiguration mechanism (from [2])

Figure 3.15 shows the torques generated once the friction models have been added to the model of the reconfiguration mechanism for the same experiment shown in Figure 3.12. Here it is possible to observe the torques generated with respect to the velocity and the position on the same graphic.

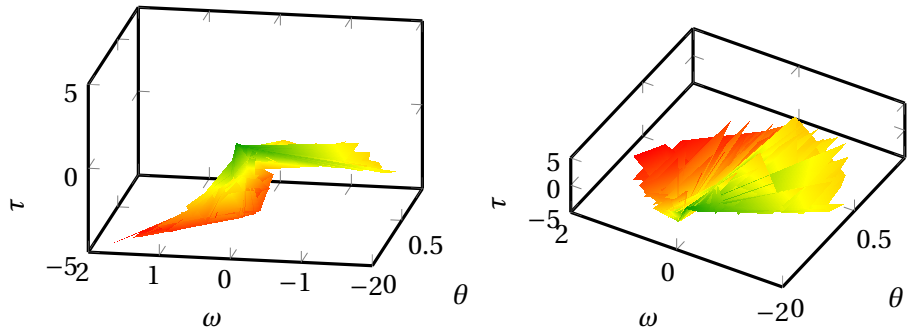

Figure 3.15: Torque generated (τ) vs position (θ) and vs velocity (ω).

Once that the friction element with the position and velocity dependent functions is added to the model, the results of the simulation are again compared to the results of the experiments in the setup. The experiment shown in Figure 3.12 was repeated, leading to the results shown in Fig 3.16. The results for experiments with low velocities in the reconfiguration mechanism are shown in Fig 3.17.

In the graphs from Fig 3.16 and Fig 3.17 the similarity between the real torque and the simulation is evident, as now the average difference is closer to zero. It is worth to mention that the torque from the experiments has not been filtered, and that the first five seconds in the simulation should be consider as initialization. From this, we can conclude that the approach taken in order to identify the non-idealities of the system was effective.

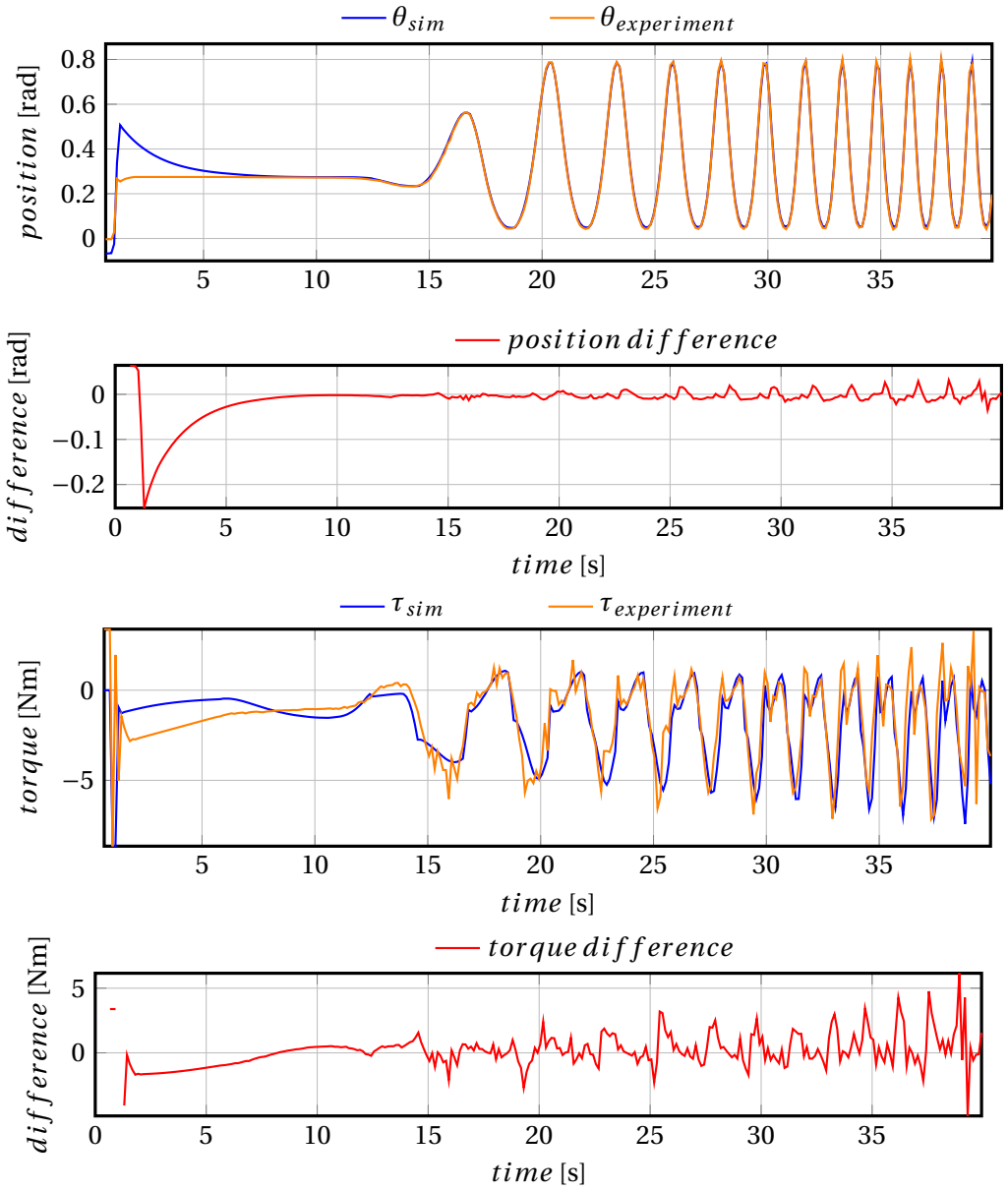

Figure 3.16: Comparison of torque and position of model with non ideal friction element vs experimental data

The aim of this model was to obtain a function that describes the non-idealities of the mechanism, so it is possible to compensate for them, using a feed-forward controller. In this case, a continues function that describes these non-idealities was obtained, which means that no neural networks (learning) are needed in the feed-forward, since a continuous function allows faster computational times, and thus, quicker responses from our controller [21].

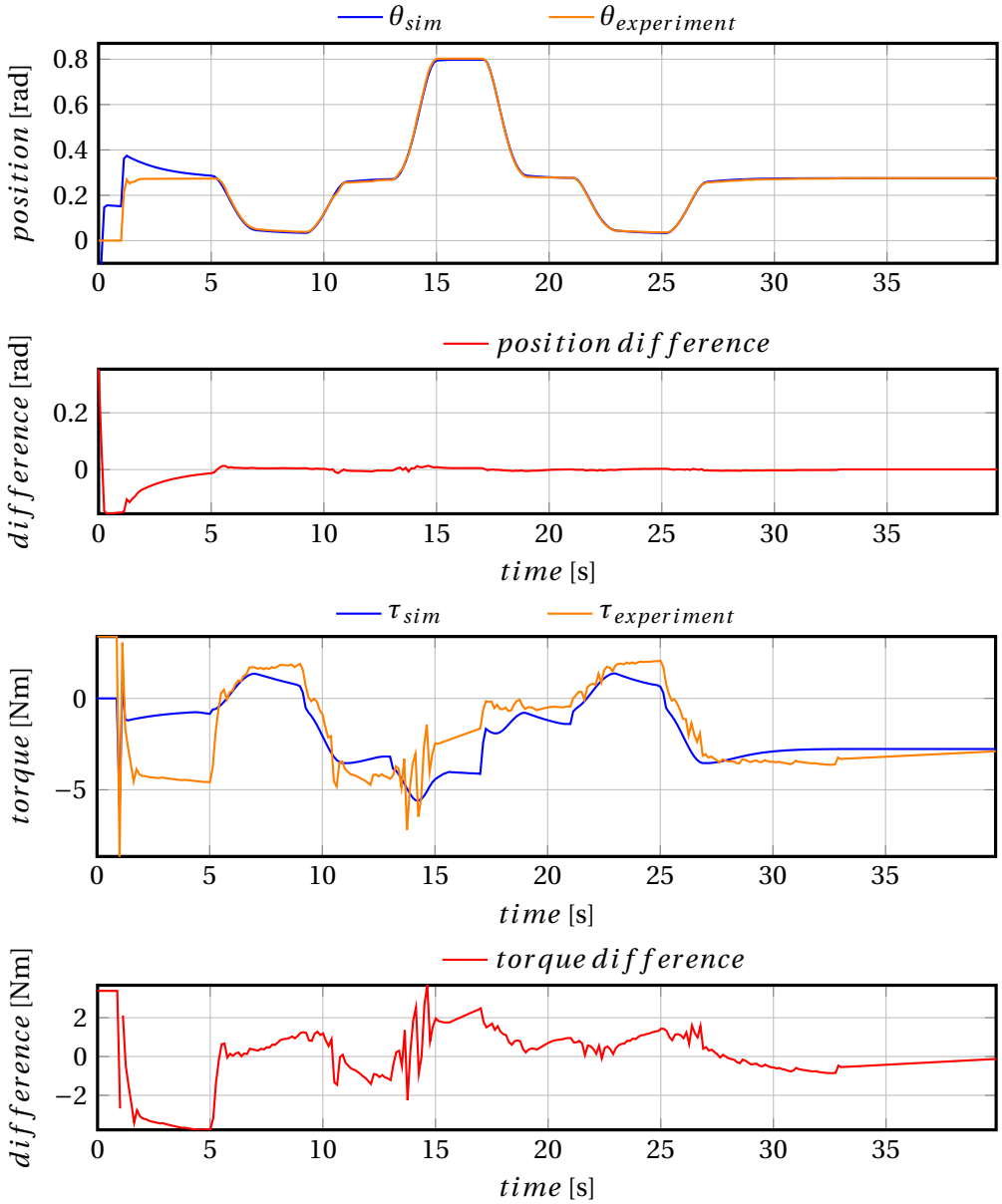

Figure 3.17: Comparison of torque and position of ideal model vs experimental data

3.4 Simplification of plant for controller design

In the previous section, a model that will help to compensate for the non-idealities of the system was developed. This friction model can be applied directly into the feed forward part of our controller. In the same way, the effects of the gravity on the mobile sphere and the gravity compensator can be considered in the feed forward of our controller. This, due to the fact that the residual forces of the spring and the gravity forces can be modeled by mathematical equations, this will be explained in Section 4.1.

Based in the information mentioned above, further simplification was made to the ideal model, in order to obtain the dynamics of the plant, and use this, as the base for the feedback controller design.

3.4.1 Bond Graph simplification

Assuming that the residual forces of the gravity compensator will be compensated in the feed forward controller, it is possible to eliminate the gravity compensator C_{gc} and the gravitational force MSe from the bondgraph in Figure 3.8, resulting in the Bond Graph shown in Fig 3.18.

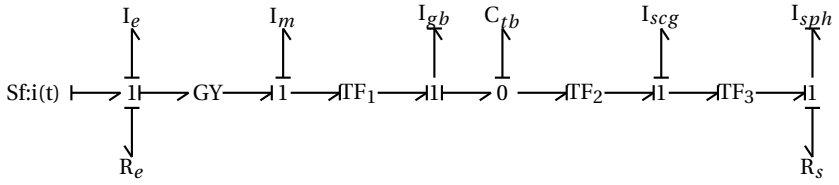

Figure 3.18: Bond graph from reconfiguration mechanism without the non ideal elements

In the previous Bond Graph all the transformers have now a constant trasmission ratio. The plant transfer function or the state space representation can be obtained, in order to use this information in the design of the controller. This will be used in the design of controllers by pole placement, which will be explained in the next chapter.

3.4.2 IPM reduction to flexible mechanism

Finally, after removing the elements which can be compensated in the feed forward control part, a further reduction of the model is possible. By means of the intuitive method, the model can be reduced to one of the elemental mechanism classes. In this case the rolling friction R_s can be neglected and all the transmissions can be eliminated, reaching the model of a Flexible mechanism, shown in Fig 3.19, where $\bar{I}_m$ is the sum of the inertias on the motor side and $\bar{I}_{sph}$ is the sum of the inertias on the end effector side; and K_{tb} is the equivalent rotational stiffness of C_{tb}.

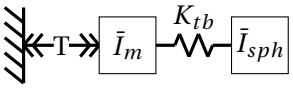

Figure 3.19: Flexible mechanism from reconfiguration system

The model in Fig 3.19 represents one class of motion system (Flexible Mechanism) [12], that describes the dynamics of the system based only in the most meaningful elements. This level of reduction is very useful when designing the controller for the plant; either using root locus or stability analysis approach. All this, due to the fact that it is possible to have transfer functions of a reduced order and with a small number of parameters, while keeping information about the dominant physical parameters in the model, taking into account the rigid body mode and the lowest mode of vibration.

With these simple, but also very useful model reductions, the modeling part of the project is considered satisfactory, and all the information and insight gained during this process will be used in the following steps of the controller design.

4 Control design

This chapter describes the approach taken to the design the motion controller for the reconfiguration mechanism based on the information obtained during the modeling process. As mentioned before, in the reconfiguration mechanism there are non-ideal behaviors, thus a model based control [22] will be used. The feed forward part of the controller will compensate of the residual forces of the spring compensator and the torques generated due to the nonlinear friction (position and velocity dependent), found in the modeling process. The feedback part will be designed as standard rigid mass controller, which will consider an ideal plant (moving mass). The controller structure is shown in Fig 4.1.

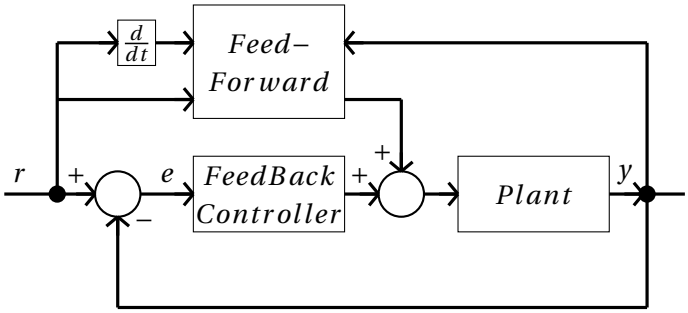

Figure 4.1: Controller structure.

4.1 Feed Forward Controller

This part of the controller is considered as model based, due to the fact that the controller can modify its behavior in response to changes in the dynamics of the process, i.e. the controller has adjustable parameters and a mechanism for adjusting them. Among the different schemes, the one implemented in the project can be considered as a Model-Reference Adaptive System (MRAS), where the performance specifications are given in terms of a reference model. This model tells how the output should respond to the command signal [22].

In this case, two models are used in the feed forward controller, the first one ($Comp_g$), will compensate for the residual forces of the gravity compensator (spring) and gravitational forces.

$$Comp_g = \tau_g + \tau_s \tag{4.1}$$

In equation 4.1, τ_g comes from equation 3.10 and the torque contribution from the spring, τ_s, can be calculated as follows.

$$\tau_s = F_s L_l \cos(\theta_0 + \phi) \tag{4.2}$$

where θ_0 and ϕ are measured as shown in Fig 3.9. This calculation requires the actual position of the system, and that is why a feedback signal is going to the adaptive control in Fig 4.1. The angle ϕ is calculated with dx and dy, from equations 3.11 and 3.12 respectively.

$$\phi = \arctan\left(\frac{dy}{dx}\right) \tag{4.3}$$

Also in equation 4.2, F_s can be found as follows.

$$F_s = F_{s0} + (L_s - L_{s0})K \tag{4.4}$$

L_s comes from 3.13, F_{s0} is equal to $-22N$, L_{s0} is equal to $132.75mm$ ($106mm$ plus the offsets on each side of the spring) and K is equal to $1800N/m$ [1].

The second model for the feed forward adaptive controller, $Comp_{fr}$ will compensate for the non-linear friction existent in the mechanism. This model depends on the desired position and velocity, which are taken from the reference. The non linear functions that describe the friction, shown in Fig. 3.13, are the following:

$$Comp_{fr} = \tau_{\omega_{ref}} + \tau_{\theta_{ref}} \tag{4.5}$$

$$\tau_{\omega_{ref}} = \begin{cases} \omega_{ref} > 0 & \tau_{\omega_{ref}} = 0.9489\omega_r + 1.7 \\ \omega_{ref} < 0 & \tau_{\omega_{ref}} = 0.1 \\ \omega_{ref} = 0 & \tau_{\omega_{ref}} = 0 \end{cases} \tag{4.6}$$

$$\tau_{\theta_{ref}} = \begin{cases} \omega_{ref} > 0 & \tau_{\theta_{ref}} = -7.3186\theta_{ref}^2 + 6.7199\theta_r + 0.1297 \\ \omega_{ref} < 0 & \tau_{\theta_{ref}} = -2.7879\theta_{ref}^2 + 2.9316\theta_r - 0.5685 \\ \omega_{ref} = 0 & \tau_{\theta_{ref}} = \tau_{\theta_{ref}} \end{cases} \tag{4.7}$$

In equation 4.7 the condition to calculate the torque takes into account the velocity ω_{ref}, because the position dependent friction is also dependent on the direction of the movement. It is possible to see that when the reconfiguration mechanism stays in the same position, the torque $\tau_{\omega_{ref}}$ keeps the same value. The θ_{ref} and ω_{ref} used in equations 4.6 and 4.7 are the desired ones (reference signals), thus equations 4.6 and 4.7 form feed forward part of the controller. In relation with Fig 4.1 $\theta_{ref} = r$ and $\omega_r = \dot{r}$.

The combination of these two models, gives the output of the Adaptive Feed Forward Controller AFF.

$$AFF = Comp_g + Comp_{fr} \tag{4.8}$$

For the Feedback controller several design methods were used in order to compare the performance of the resulting controllers. This will be explained in section 4.2.

4.2 Feedback Controller Design

The desired controller for the reconfiguration mechanism should have a robust tracking and disturbance rejection. In the previous section (4.1) a controller that is able to cope with the non-idealities (disturbances) of the reconfiguration mechanism was found. Based on this premise, the feedback controller must deal with the control of the plant, considering it as ideal.

Nowadays, there exist many control strategies options, each of them has its advantages and disadvantages. A well known control system to achieve robust servomechanisms is the PID controller. Thus, the feedback controller for the reconfiguration mechanism will be designed using a PID controller structure. Taking advantage of the simple and systematic design procedures for this type of controllers. A PID series algorithm will be design using the rules of thumb mentioned in 2.3.1.2. The parallel PID algorith is also choosen due to the flexibility during its design. The ideal algorithm was not implemented, as not an specific tuning procedure is preferred.

4.2.1 Plant

As mentioned before the plant used for the design of a feedback control is considered to be ideal, as shown in Fig 3.18 and 3.19. Nevertheless, it is necessary to check if the information that this plants (complete plant and flexible mechanism) give us is sufficient and of good quality to design a controller based on it.

From the bond graph in Fig 3.18 we can obtain the following state space representation of the system [5].

$$A = \begin{pmatrix} 0 & \frac{-1}{I_m - n_1^2 I_{gb}} & 0 \\ \frac{n_1}{C_{tb}} & 0 & \frac{-n_2 n_3}{C_{tb}} \\ 0 & \frac{n_2 n_3}{I_{sph} + n_3^2 I_{scg}} & \frac{-I_{sph} R_s}{I_{sph} + n_3^2 I_{scg}} \end{pmatrix} \tag{4.9}$$

$$B = \begin{pmatrix} \frac{r_{GY}}{I_m - n_1^2 I_{gb}} \\ 0 \\ 0 \end{pmatrix} \tag{4.10}$$

$$C = \begin{pmatrix} 0 & 0 & 1 \end{pmatrix} \tag{4.11}$$

$$D = \begin{pmatrix} 0 \end{pmatrix} \tag{4.12}$$

After value substitution is possible to know that the rank of the A matrix is 3 (full rank). Nevertheless, the condition number of the matrix is very high (1781624071.5), meaning that there is a high correlation between the rows of the matrix, i.e. there is a dependency on the states of the storage elements. Also the controllability matrix R for system:

$$R = \begin{pmatrix} B & AB & A^2 B \end{pmatrix} \tag{4.13}$$

is not full rank ($rank = 2$). From this we can say that considering all the elements in the bond graph as the plant for our controller is not a good approach.

Reducing the model of the plant to one of the classes of motion systems (four order plants), as shown in Fig 3.19, is possible to get useful information about the plant. Since the class of the electromechanical system is a flexible mechanism, and the the feedback signal is representing the angular position of I_{sph}, then the transfer function for the four order plant is of type R, and it has a resonance frequency $\omega_r = 67288\ rad/s$, which is a very high value compared to the desired crossover frequency $\omega_c \approx 100\ rad/s$, which according to the stability analysis condition for the transfer function type R ($\omega_r > 4 \times \omega_c$), the system is stable.

It is possible to say that the high value for the resonance frequency is the result of the relatively high value of the stiffness ($K_{tb} = 125460750\ Nm/rad$) compared to the inertias ($I_m = 0.043445835\ kgm^2/rad$ and $I_{sph} = 0.07649972449\ kgm^2/rad$). This means that the connection between the two inertias can be consider as rigid, and thus, the plant can be consider as a single moving inertia with the following transfer function.

$$P(s) = \frac{1}{I_{total} s^2} \tag{4.14}$$

The plant described by equation 4.14 will be used during the design of the Feedback controller. The total inertia is $I_{total} = 0.119945559\ kgm^2/rad$.

4.2.2 Series or interacting PID

The first method selected for the Feedback controller, is designing a series (interacting) PID controller, as the one presented in section 2.3.1.2, also using the mentioned rules of thumb of the stability analysis approach.

With this in mind, several controllers were designed and tested using different crossover frequencies ω_c. The chosen frequency, $\omega_c = 100\ rad/s$, was the one with the best behavior, i.e. with better speed response and better accuracy when tracking the set point.

The design procedure of the PID controller starts once the total mass or inertia of the plant and the desired crossover frequency are known. Since this data is already available, the calculation of the proportional gain K_p and the time constants can be done to start the tuning of the PID controller as follows:

$$K_p = \frac{\omega_c^2 I_{total}}{\sqrt{\beta}} = \frac{100^2 \times 0.119945559}{\sqrt{10}} = 379.3 \tag{4.15}$$

$$\tau_z = \sqrt{\beta}\frac{1}{\omega_c} = \sqrt{10}\frac{1}{100} = 0.031 \tag{4.16}$$

$$\tau_p = \frac{1}{\sqrt{\beta}\omega_c} = \frac{1}{\sqrt{10} \times 100} = 0.0031 \tag{4.17}$$

$$\tau_i \geq \sqrt{\beta}\frac{2}{\omega_c} \geq \sqrt{10}\frac{2}{100} \geq 0.062 \tag{4.18}$$

Finally, according to the obtained quantities, the controller's transfer function is given by:

$$C(s) = K_p \cdot \frac{s\tau_z + 1}{s\tau_p + 1} \cdot \frac{s\tau_i + 1}{s\tau_i} = 379.3 \cdot \frac{0.031s + 1}{0.0031s + 1} \cdot \frac{0.062s + 1}{0.062s} = \frac{0.73s^2 + 35.275s + 379.3}{1.92 \times 10^{-4}s^2 + 0.062s} \tag{4.19}$$

With the obtained model from Chapter 3, the feed-forward from equation 4.8 and the feedback controller shown in equation 4.34, the structure from Figure 4.1 was implemented in 20-sim. Simulations are shown in Figure 4.2.

Even though it is possible to see that the maximum tracking error, after five seconds, is around 0.0005 rad, there is a high overshoot (40%) when the controller begins to actuate. Because of this large displacement, when this controller is used in the setup, the moving arm will most likely move abruptly and probably hit one of the end stops. If this happens, there could be disturbances or damages to the sensors which are fixed on the structure. For this reason, the displacement at start-up should keep a distance of at least 0.5 rad away from the end stops. Besides that, large displacements during operation are not desired, and there is the possibility that the transmission ratio needs to be changed in large values. Thus, to decrease the big displacements, it is desired to limit the gains of the controller at lower frequencies. This can be done by increasing τ_i, so the integral action stops earlier, which was achieved by tuning it to a value of 0.562s, which is very high compared to value obtained in equation 4.18.

As an extra measure to avoid the high overshoot when using this controller, a change in the initialization procedure of the setup was implemented. This is described in Appendix B.

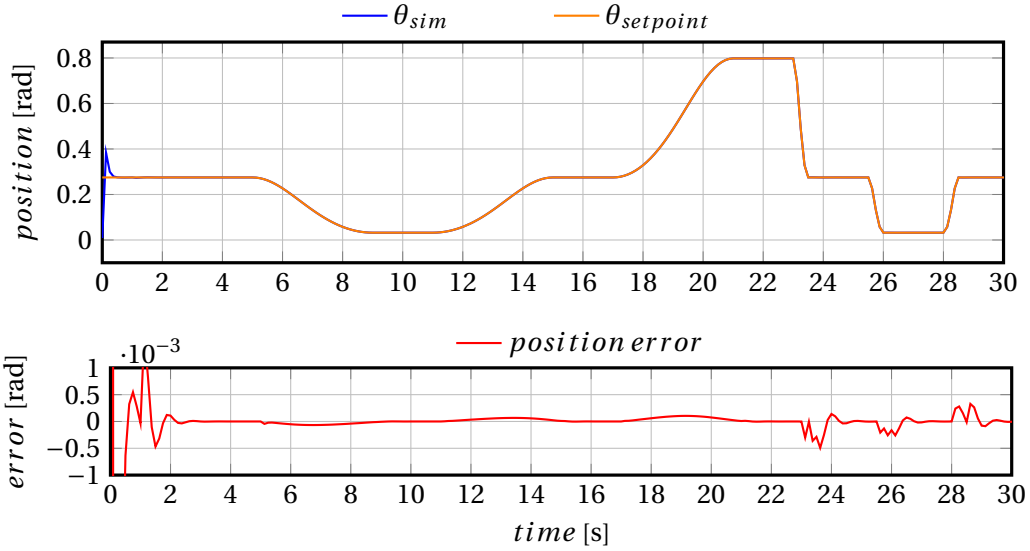

Figure 4.2: Series PID controller simulation

The change in the controller behavior can be seen in Figure 4.3. It is possible to observe how the magnitude at low frequencies now is smaller and the phase advance starts also, at very low frequencies.

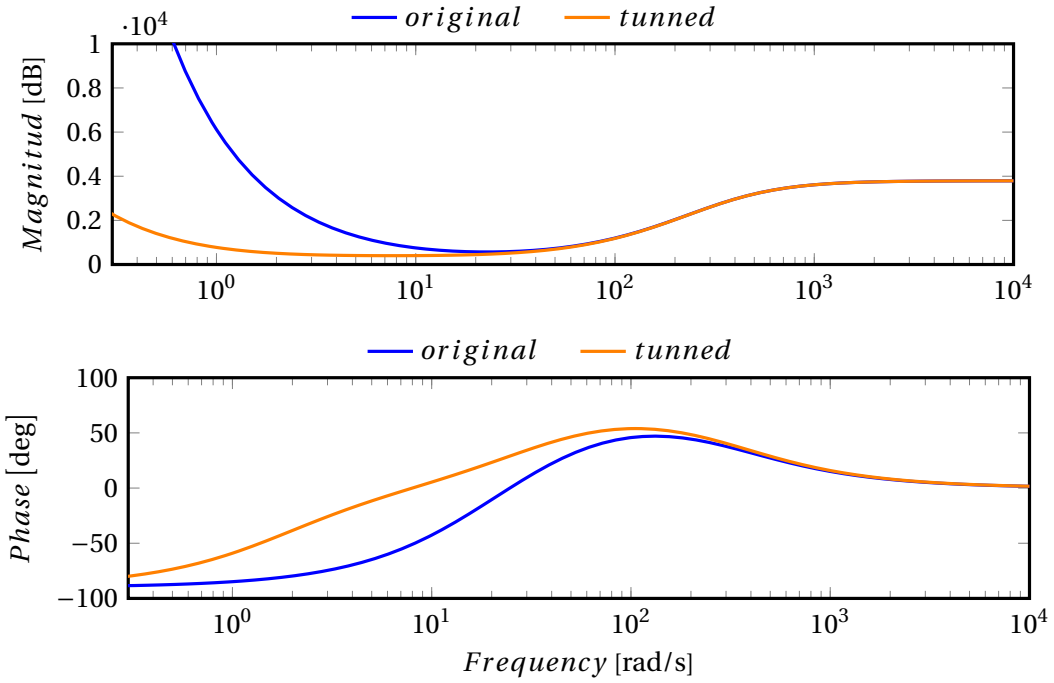

Figure 4.3: Bode Plot PID controllers with 100 rad/s bandwidth

The controller transfer function is changed as follows:

$$C(s) = K_p \cdot \frac{s\tau_z + 1}{s\tau_p + 1} \cdot \frac{s\tau_i + 1}{s\tau_i} = 379.3 \cdot \frac{0.031s + 1}{0.0031s + 1} \cdot \frac{0.562s + 1}{0.562s} = \frac{0.73s^2 + 35.275s + 379.3}{0.3158s^2 + 0.562s} \quad (4.20)$$

The simulation of the modified controller gave the results shown in Figure 4.4. Where we can see how the overshoot has been reduced, and the risk of crashing with the end stops does not

exist any more. Besides the maximum error in the position of the reconfiguration mechanism is about $0.002 rad$, which represents 0.25% of the operational range. With these results both controllers were tested in the setup, with the corresponding precautions to avoid damage on the setup, when testing the first one.

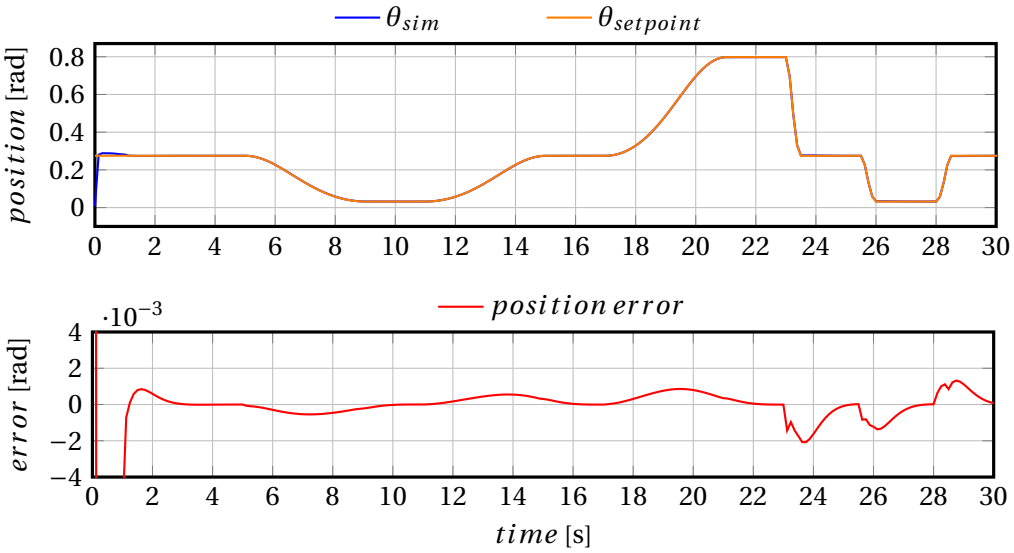

Figure 4.4: Modified Series PID controller simulation

4.2.3 Parallel or non-interacting PID

In this section a more pragmatic approach for the design of the controller is will be explored. This consists on designing a parallel (non-interacting) PID as the one mentioned in section 2.3.1.1.

In this approach it is possible to keep the value of K_p obtained in section 4.2.2, due to the fact that it is related to the plant which remains the same.

Looking at the resonance peak, which occurs at an infinite gain of the complementary sensitivity function, we have:

$$T(s) = \frac{P(s)C(s)}{1+P(s)C(s)} = \frac{K_p/I_{total}s^2}{1+K_p/I_{total}s^2} = \frac{K_p}{K_p + I_{total}(j\omega)^2} \tag{4.21}$$

$$\frac{K_p}{K_p + I_{total}(j\omega)^2} \div K_p \Rightarrow \frac{1}{1 - \frac{I_{total}}{K_p}\omega^2} \tag{4.22}$$

At resonance frequency, it is possible to see that ω_c is given by:

$$\omega_c = \sqrt{\frac{K_{spring}}{m}} = \sqrt{\frac{K_p}{I_{total}}} \tag{4.23}$$

Based on equation 4.23, it is possible to see that K_p acts as a virtual spring. Furthermore, critical damping in a second order plant occurs under the circumstances given by equation 4.24:

$$critical\ damping = 2\sqrt{K_{spring}m} = 2\sqrt{K_p I_{total}} \tag{4.24}$$

Based on the affirmation that K_p behaves as a spring, using the critical damping described and adding the damping ratio parameter (ζ) it is possible to calculate the desired virtual damping (K_d) of the system, as shown in equation 4.25:

$$K_d = 2\zeta\sqrt{K_p I_{total}} = 2 \cdot 0.7 \cdot \sqrt{379.3 \times 0.119945559} = 9.44 \tag{4.25}$$

The damping ratio parameter (ζ) was chosen equal to 0.7, based on equation 4.26 [23], which relates the percentage overshoot to the value of ζ. Thus this value results in a reasonable overshoot (less than 10%) being a good compromise between rise time and settling time.

$$\zeta = \frac{-\ln(\%OS/100)}{\sqrt{\pi^2 + \ln^2(\%OS/100)}} \tag{4.26}$$

With respect to integral action, the gain was tuned manually with the aid of simulations and choosing the one that yielded the best results. The selected value is $K_i = 20$.

To obtain the PID parallel controller, equation 4.27 is used. Moreover, the canonical form of the controller is given by equation 4.28.

$$C(t) = K_p e + K_d \dot{e} + K_i \int e = 379.3e + 9.44\dot{e} + 20 \int e \tag{4.27}$$

$$C(s) = \frac{K_d s^2 + K_p s + K_i}{s} = \frac{9.44s^2 + 379.3s + 20}{s} \tag{4.28}$$

Since the Parallel algorithm results in a non proper transfer function, is not possible to analyze the behavior of the controller by means of a bode plot, like we did with the Series PID algorithm. Nevertheless, it is possible to take advantage of the simulation tools to check the behavior of the system when this controller is applied. The results of the simulation are shown in Figure 4.5.

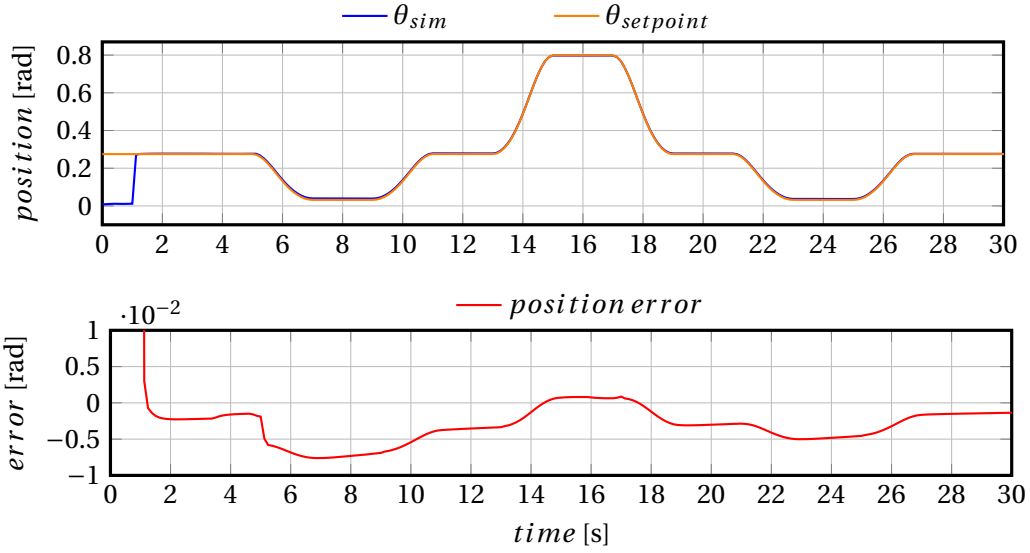

Figure 4.5: Modified Series PID controller simulation

In Figure 4.5 it is possible to observe that the designed controller does not have any overshoot, and the maximum error is less than $0.0075 rad$, which represents around 1% of the operational range of the reconfiguration mechanism. Thus, this controller was considered as a good candidate to be the final controller for the reconfiguration mechanism.

4.3 Comparison of designed controllers

In this section a comparison between the designed controllers is presented, given the fact that they have been tuned using two different algorithms. Nevertheless, the difference between these algorithms is how the Proportional, Integral and Derivative gains affect each other. Taking into account that two controllers are in the series form, an equivalence for the Parallel PID controller to a Series PID controller was obtained as described in [24]. The first step is to get the equivalence from the Parallel PID to the ideal PID, because they are very similar, the equations that describe the Parallel PID (left) and Ideal PID (right) controllers are shown in equation 4.29.

$$C_{cp}(s) = K_{cp} + \frac{1}{T_{ip}} + T_{dp}s \quad \Rightarrow \quad C_{ci}(s) = K_{ci}\left(1 + \frac{1}{T_{ii}s} + T_{di}s\right) \tag{4.29}$$

From equation 4.29, the following equivalences are obtained:

$$K_{ci} = K_{cp} \qquad T_{ii} = T_{ip}K_{cp} \qquad T_{di} = \frac{T_{dp}}{K_{cp}} \tag{4.30}$$

Solving this equations with the data from the Parallel PID controller we obtain:

$$K_{ci} = 379.3 \qquad T_{ii} = 0.05 \times 379.3 = 18.965 \qquad T_{di} = \frac{9.443}{379.3} = 0.02489 \tag{4.31}$$

Then, the ideal controller gains can be transformed to series controller gains, according to [24], if $T_{ii} > 4Tdi$, it can be shown:

$$K_{cs} = 0.5K_{ci}\left(1 + \sqrt{1 - 4\frac{T_{di}}{T_{ii}}}\right), \quad T_{is} = 0.5T_{ii}\left(1 + \sqrt{1 - 4\frac{T_{di}}{T_{ii}}}\right), \quad T_{ds} = 0.5T_{di}\left(1 + \sqrt{1 - 4\frac{T_{di}}{T_{ii}}}\right) \tag{4.32}$$

Solving with the values obtained in equation 4.32:

$$K_{cs} = 378.8, \qquad T_{is} = 18.94 \qquad T_{ds} = 0.02485 \tag{4.33}$$

After obtaining the values for the gains of the Series PID controller they can be substituted in the equation 4.34, where $tau_z = T_{ds}$, $\tau_i = T_{is}$, $K_p = K_{cs}$ and $tau_p = 0.1 \times T_{ds}$, obtaining the following transfer function:

$$C(s) = \frac{178.5726s^2 + 7183.9s + 378.8}{0.04714s^2 + 18.94s} \tag{4.34}$$

Once that all the controllers were represented as the same type of controller, it was possible to compare the behavior of the three designed controllers. This is shown in Figure 4.6, where we can observe that all the controllers have a crossover frequency of $100rad/s$ (where the maximum phase lead occurs). It is observable that in the Parallel PID controller the integral action stops earlier, and the damping action starts also at lower frequencies, while all the controllers have the same behavior after the crossover frequency.

Furthermore, the closed loop stability of the controllers was tested for the plant from equation 4.14, obtaining the results shown in Figure 4.7 in a Nichols chart. In the Figure we can observe that all the controllers have a stable behavior, being the Series PID 1 the one that is closer to the unstable region (circle of 6dB gain for complementary sensitivity function). Given the fact that the plant is being considered as ideal, special attention is needed for the experiments, as the non idealities are totally compensated with the models obtained in section 3.3.

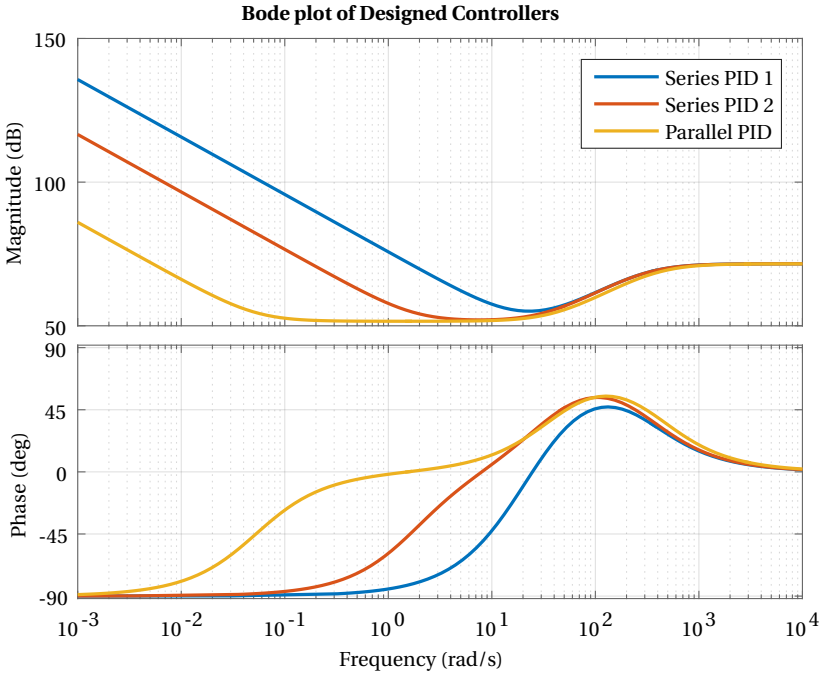

Figure 4.6: Bode chart of designed controllers.

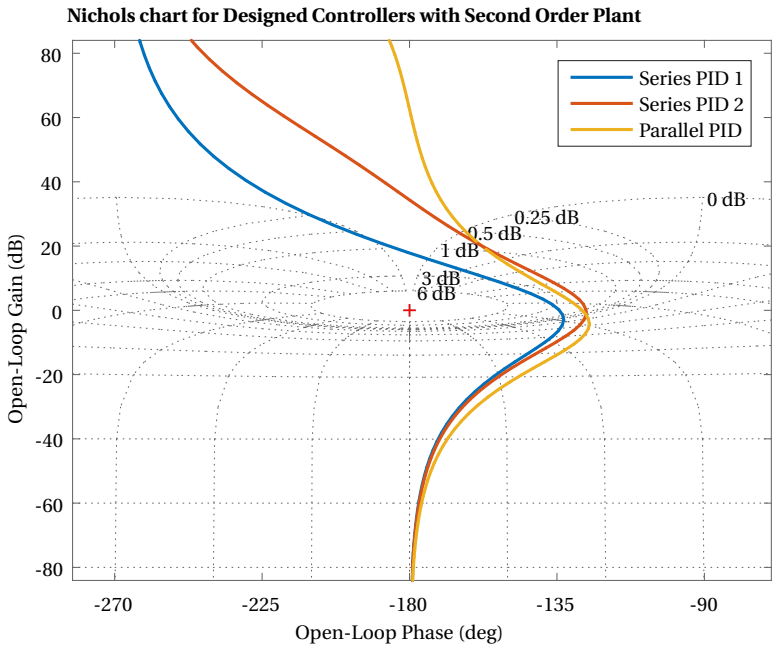

Figure 4.7: Nichols plot of controllers combined with second order plant.

5 Results

This chapter shows the results obtained with the designed controllers from Chapter 4. As mentioned earlier, the adaptive feed-forward controller will be combined with the two selected feedback controllers. In general, this chapter provides an overview of the different experiments that were made and an analysis on the observed responses.

5.1 Experiment description

As a starting point, the basic information of the performance, i.e. settling time, overshoot, steady state error, etc., will be obtained through a step response experiment. This will be described in Section 5.2

In order to further test the performance of the designed controllers in the setup, two other experiments are proposed. The first one, aims to provide insight on the performance of the controllers throughout the transmission ratio ranges. Because of this, it only involved the reconfiguration mechanism part of the system. This first experiment, consisted in varying the transmission ratio starting at zero and modifying the values to either side of the range (-3.5 or 3.5) using different speed rates in between the changes. This experiment is referred to as ratio control and will be discussed in Section 5.3.

Nonetheless, to provide experimental evidence about the behavior of the controllers in combination with the whole system (not only the reconfiguration mechanism), a more thorough examination is proposed. This involved connecting our designed controllers to the reference provided by the output position controller, which was developed and discussed in [10]. In this case, we would like to compare the tracking error for each of the controllers with respect to the current one. This final experiment will be explained in Section 5.4.

5.2 Step response

Because of the insight that it provides on the basic performance of a controller, the first experiment involved a step response analysis. To do so, a reference was sent to the system requesting a zero transmission ratio. As seen in Figure 3.9, the initial position of the arm is very close to zero degrees (transmission ratio ≈3.5). With this experiment the system is requested to make a movement equivalent to 50% of the transmission ratio range (from 3.5 to 0) instantaneously, i.e. a step. During this test, it will be possible to observe if the system overshoots or is overdamped (and to which extent), and also to obtain a quantitative result of the steady state error. The results of the experiment carried out in the setup are shown in Figures 5.1, **??** and 5.4.

As it is visible in Figure 5.1, the existent controller has a settling time of approximately 0.7s and a small overshoot (≈ 5%). The steady state error is approximately $0.002 rad$ (≈ 0.25%), which is quite acceptable. Nonetheless this controller's response was lacking in other kind of experiments, such as ratio and position control, which will be presented in Sections 5.3 and 5.4, respectively.

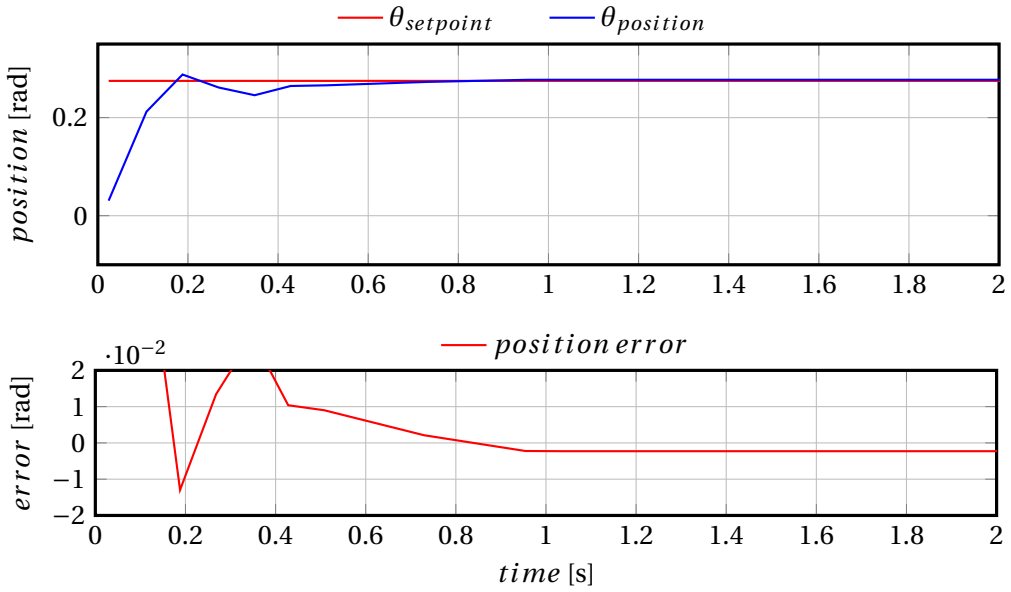

Figure 5.1: Step response using existent controller

The first designed control (Series PID 1), a series PID controller with a feed forward, and tuned with the rules of thumb previously mentioned, gave the results shown in Figure 5.2. In the plot is possible to see that the settling time is approximately $0.55 sec$ and it has an overshoot of around 48%. This means that compared to the previous (existing) controller, it is slightly faster, however the steady state error in this controller does reach value very close to zero ($0.0002 rad \approx 0.02\%$ of the operational range).

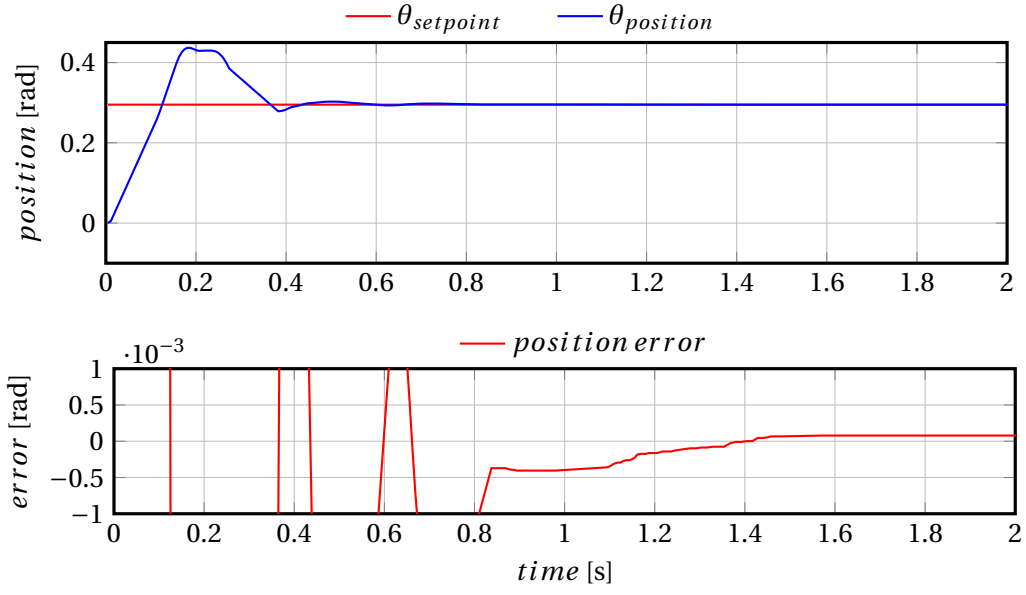

Figure 5.2: Step response using Series PID 1 and feed forward

The results for the second designed control (Series PID 2), a series PID controller with τ_i tuned manually, and with a feed forward, are shown in Figure 5.3. This time it is possible to see that the settling time is approximately $1.2 sec$ and it has an overshoot of around 6.8%, which is very low compared to the previous controller (seven time less overshoot). This means that compared to the existing controller, it is slightly slower. The steady state error for this controller reach a value of $0.003 rad \approx 0.4\%$ of the operational range.

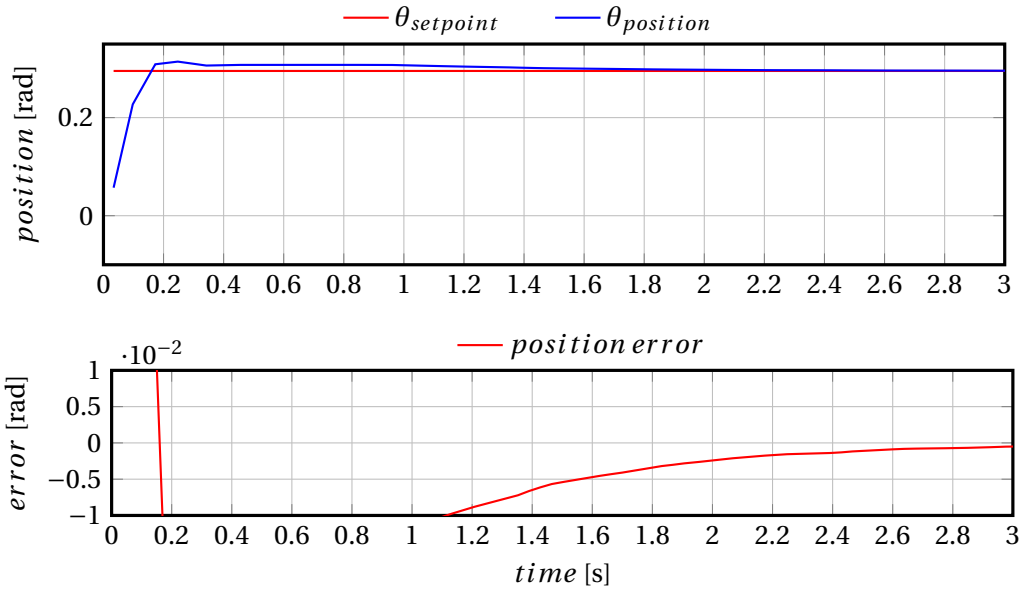

Figure 5.3: Step response using PID Series with τ_i manually tuned and feed forward

The third controller design consisted of a parallel PID also with feed forward. The settling time obtained with this controller is around $0.6s$ and behaves as an overdamped system. Under this conditions, the steady state error resulted in approximately $0.006rad$ which accounts for 0.77%.

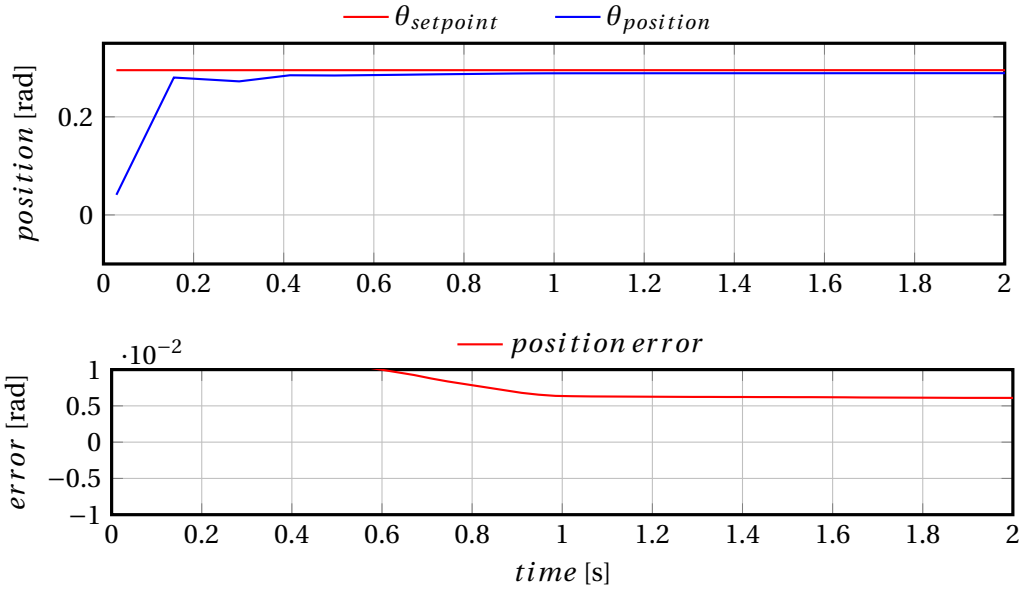

Figure 5.4: Ratio control using PID Parallel and feed forward

Comparing these four different controllers, it is possible to conclude that there is an observable trade-off between accuracy and settling time or overshoot. This means, in the first scenario, that the fastest controller (parallel PID) obtains also the greatest steady state error and the slowest one (series PID 2) does achieve very low error. In the second scenario, a fast and accurate system, gives a very high overshoot, which is not desirable. Due to this trade-off, it is not possible to thoroughly compare, using this experiment alone, the performance of these controllers. In the next sections, the other experiments that were carried out will be described.

5.3 Ratio control

Another important performance factor for the current work is the accuracy of the tracking throughout all the working transmission ratio range and at different speeds.

The aim of this experiment was to check the quality of the tracking under extreme changing conditions, which under normal usage will not be required. In this way, we would make observations in the worst case scenario and therefore test each of the controllers' robustness.

The results for the three controllers (in the same order as presented above) are shown in Figures 5.5, 5.6, 5.7 and 5.8.

When the previously existing controller was subjected to this test, the results showed that the tracking response at start-up (during the first 5 seconds) is very good. However, when the reference signal is (abruptly) changed, the tracking quality decays, presenting errors greater than 4%. This can represent a variation of $0.33Nm$ for force actuation, which is considerable.

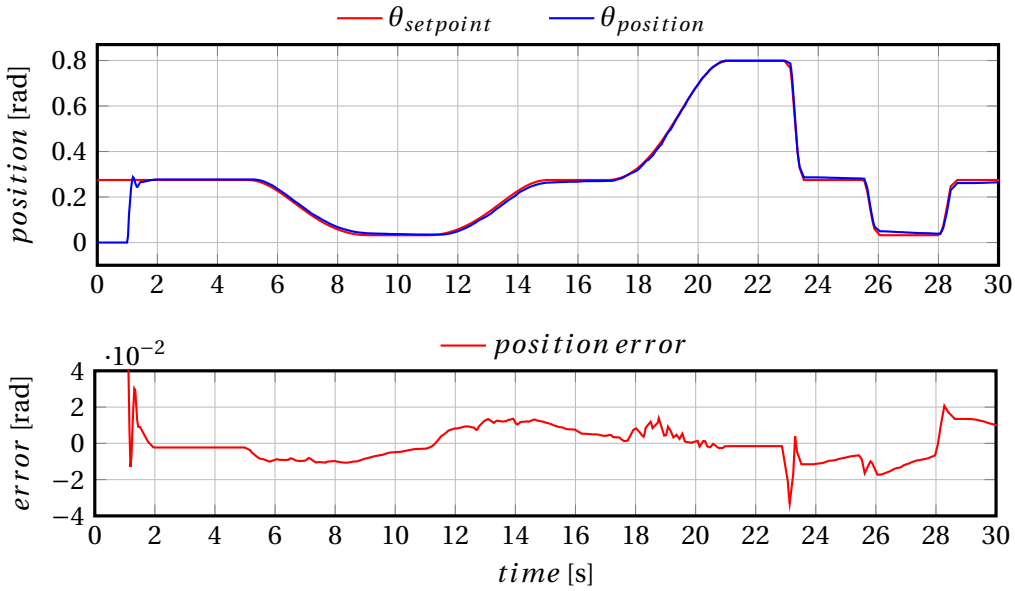

Figure 5.5: Ratio control using existent controller

Based on the results from step response experiment shown in Section 5.2, the expectancy for the series PID controllers that were designed, is that the quality of the tracking should be improve with respect to the existing one. It can be seen in Figure 5.6, for the controller without modification (Series PID 1), that this effectively is the case. Under the same conditions of abrupt transmission ratio changes and speed variation, this controller presents an error no greater than 0.65%. In the second graph, where the error in position is plotted, we can observe that the average is very close to zero, which means that it responds well to any changes. This attests to very good tracking accuracy and precision.

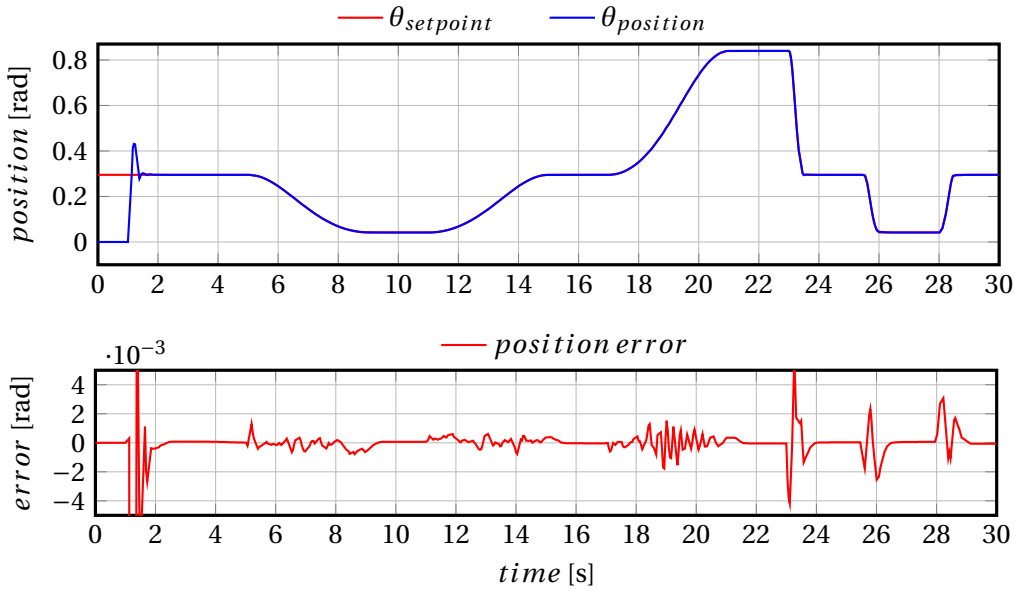

Figure 5.6: Ratio control using PID Series without modification and feed forward. Plot shows the position of the reconfiguration mechanism.

In Figure 5.7, the results using the Series PID controller with a tuned τ_i (Series PID 2) are shown. Under the same conditions, this controller presents an error no greater than 1%. We can observe that, for this controller, the average error is also very close to zero. If a comparison between Fig. 5.6 and 5.7, is is visible that the tuned controller has a smoother behavior, based on the fluctuations of the error.

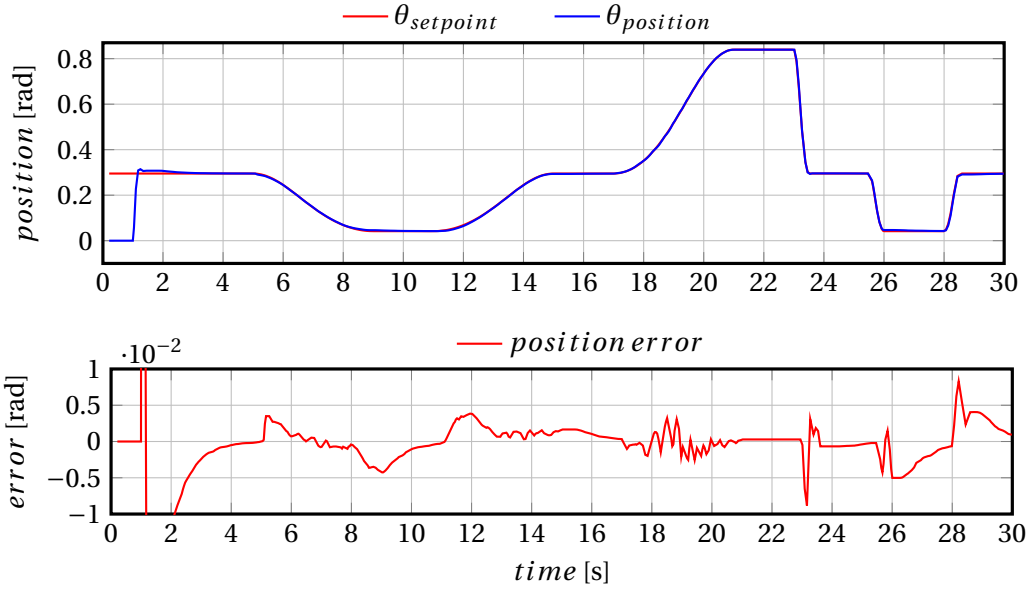

Figure 5.7: Ratio control using PID Series with τ_i tuned and feed forward. Plot shows the position of the reconfiguration mechanism.

Finally, the test was performed using the parallel PID controller. From the results in Section 5.2 it was expected for this controller to have bigger error than the previous ones. Nevertheless, the test results in Figure 5.8, showed a maximum tracking error $\approx 1\%$, which is very good. However, it can be observed that the error remains $\neq 0$ throughout most of the experiment, which is not desirable.

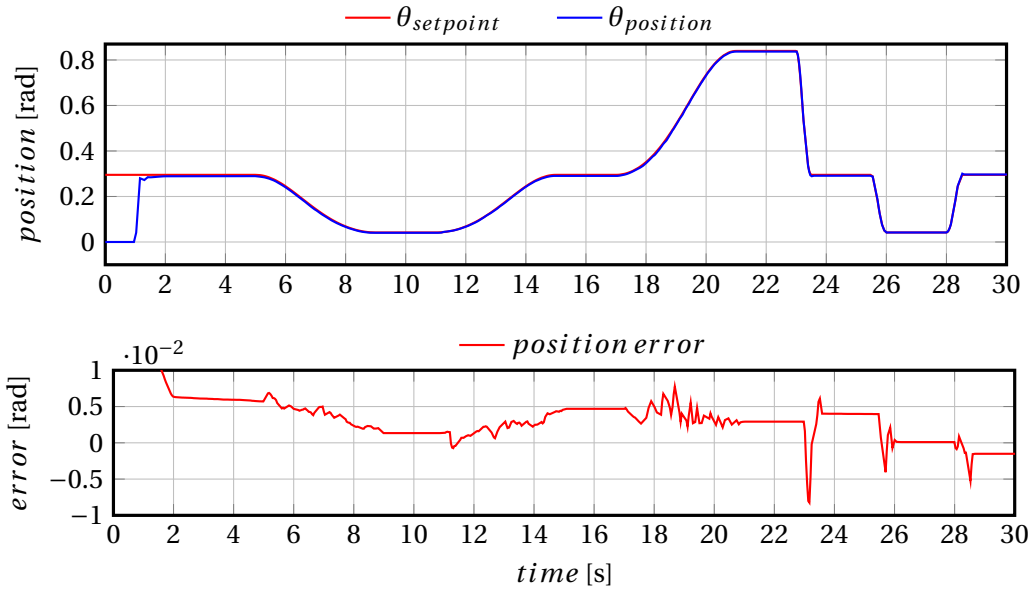

Figure 5.8: Ratio control using PID Parallel and feed forward. Plot shows the position of the reconfiguration mechanism.

During this experiment, it was possible to observe that the three designed controllers have a better performance than the existing one. With the series PID controllers (1 and 2) standing out, due to the low values of error achieved through the whole range of possible position for the reconfiguration system. A final experiment, discussed in Section 5.4, will test the controllers for standard operation conditions in a controlled passive actuation scheme.

5.4 Load Position Control

As explained before, in this experiment the existing and the three designed controllers will be tested for position control of the load, taking as input the reference generated by the output position controller developed in [10]. This will give an idea of the performance of the controllers for the standard operation of the Dual-Hemi CVT in a controlled passive actuation scheme. Figure 5.9 depicts the control structure used for the load position control. In it, the load position controller outputs a signal for force actuation, then a force controller calculates the required transmission ratio to reach the desired force, and finally the desired ratio is converted to a position for the reconfiguration mechanism and fed into the controller, which will be tested during this experiment.

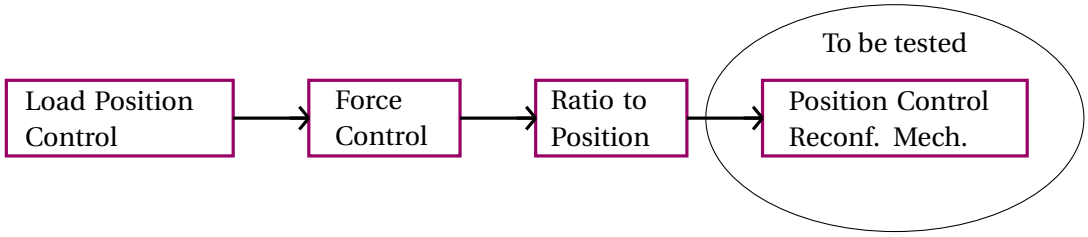

Figure 5.9: Load position control signal flow diagram.

The results of the experiment are shown in Figures 5.10, 5.11, 5.12 and 5.13. The reference signals, in this case, are different as they are generated in real time the position-force controller of the Dual-Hemi CVT.

When the existing controller was subject to the position control experiment, it the results were very similar to the ones in the ratio control experiment, they can be observed in Figure 5.10. A maximum error of ≈ ±5% was reached, which is not desirable for force actuation.

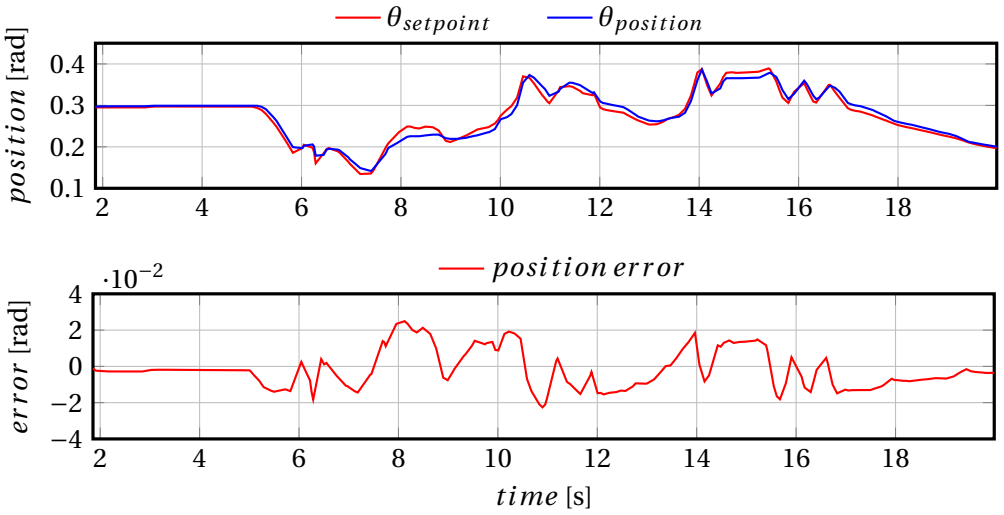

Figure 5.10: Position control using existing controller. The plot shows the position of the reconfiguration mechanism.

The Series PID without modification (Series PID 1), had a performance very similar to the one obtained in the ratio control experiment, in the plot shown in Figure 5.11. Nevertheless the behavior for this controller was not as good as expected during the test, as it make the system unstable for most of the trials, even though the sample frequency was incremented at twice the value that all the other controllers use to work without any problem. However, during a successful trial, it is possible to see that the error remains ≈ ±1%.

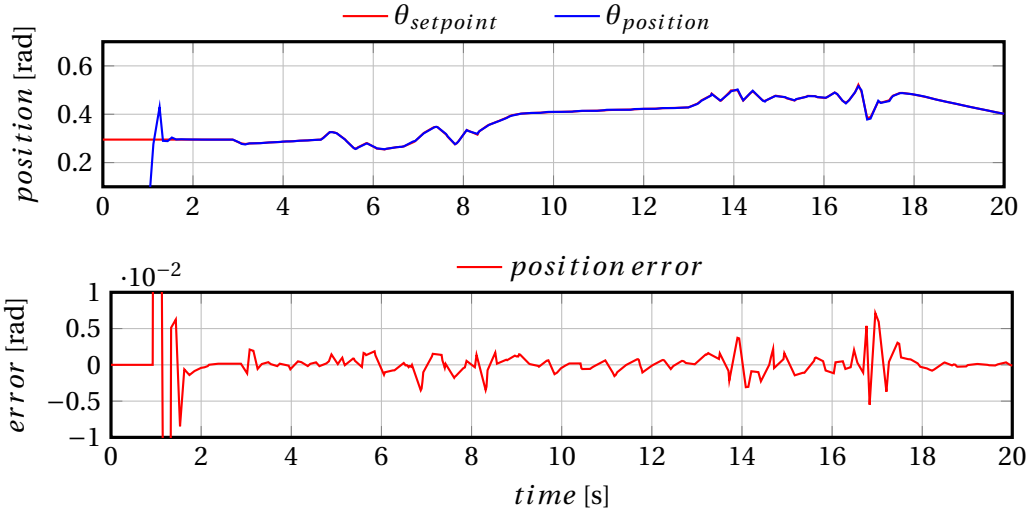

Figure 5.11: Position control using PID Series and feed forward. The plot shows the position of the reconfiguration mechanism.

The Series PID controller with tuned τ_i (Series PID 2), had a performance very similar to the one obtained in the ratio control experiment. The position control results are shown in Figure 5.12. It is possible to see that the error also remains ≈ ±1% with an average value very close to zero, thus with a very high quality in tracking accuracy. This controller, unlike the previous, had a very stable behavior during all the experiments carried out.

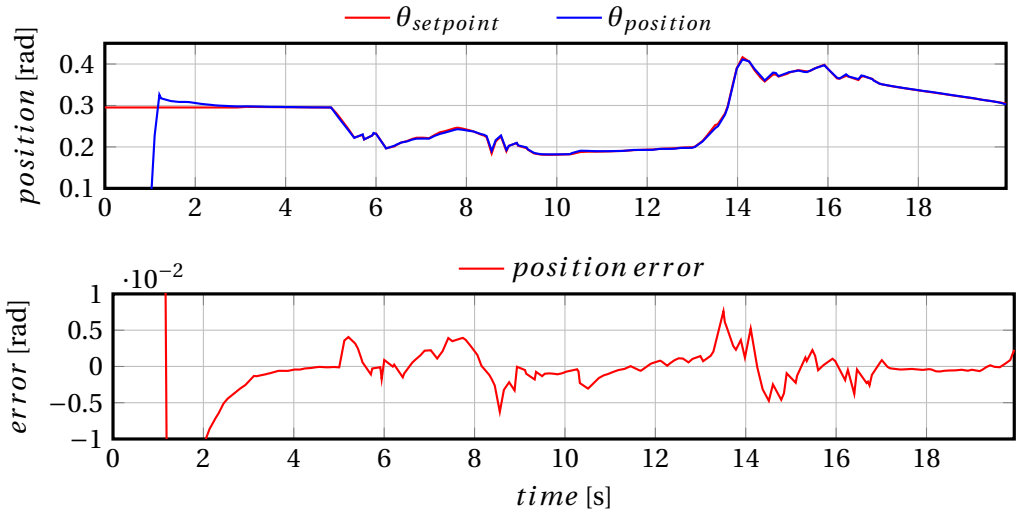

Figure 5.12: Position control using PID Series and feed forward. The plot shows the position of the reconfiguration mechanism.

In figure 5.13 the position control results for the parallel PID controller are shown. It can be observed that the behavior from previous experiment also holds in this case. The maximum error stays $\approx \pm 1\%$ with an average value $\neq 0$. However, the tracking performance of this controller is considerably better than the existing one.

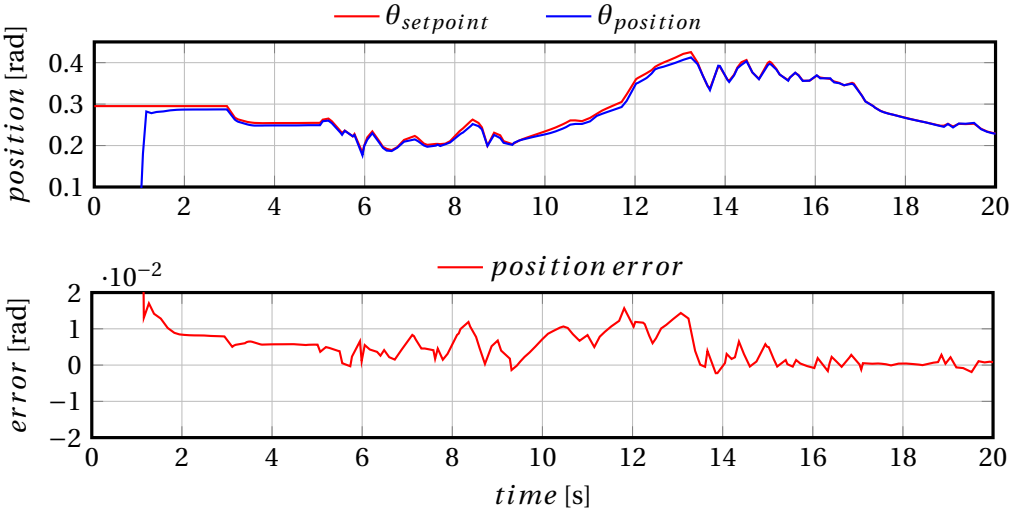

Figure 5.13: Position control using PID Parallel and feed forward. The plot shows the position of the reconfiguration mechanism.

This experiment showed again that the combination of the adaptive feed forward controller combined with the Series PID 2 gives an outstanding performance over the existing and Parallel PID controller, and in this case, a much better behavior than the Series PID 1, since the last one have unstable behaviors during the experiments. The effect of the controllers can also be observed in the load position, as shown in Figures 5.14, 5.15, 5.16 and 5.17. It is remarkable that the performance obtained by the Series PID 1 controller was not repeated in most of the trials.

In Figure 5.14 we can observe large errors in the desired final position of the load, produced by the significant errors in the transmission ratio (dependent of the position of the reconfiguration mechanism).

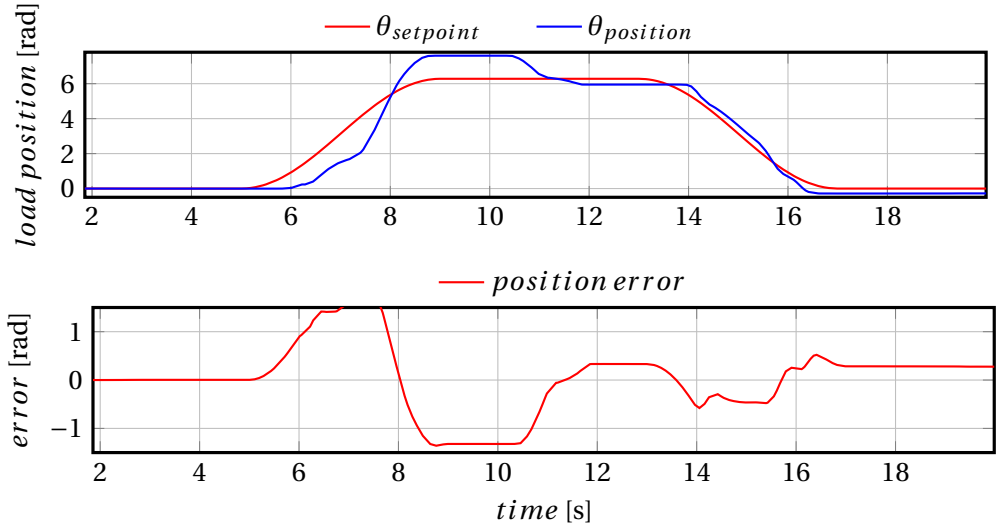

Figure 5.14: Position control using existing controller. The plot shows the load position.

For the PID series controller without modification (Series PID 1), the error in the final desired position of the load was ≈ 0, which reflects a good performance of the reconfiguration mechanism controller. Nevertheless, as mentioned before, this controller had unstable behaviors in most of the trials. Successful results are shown in Figure 5.15.

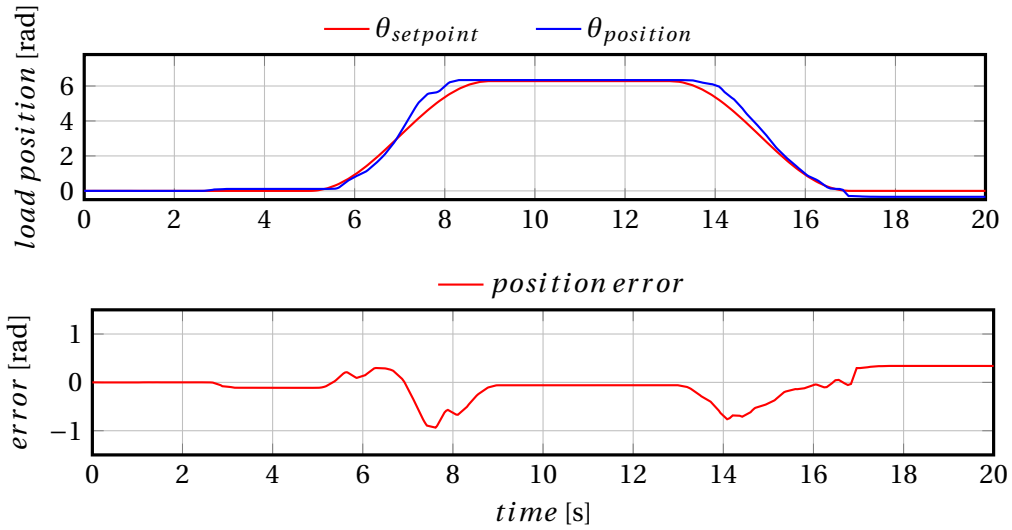

Figure 5.15: Position control using PID series controller without modification for reconfiguration system. The plot shows the load position.

Using the PID series controller with τ_i tuned (Series PID 2), the error in the final desired position of the load was also ≈ 0, which reflects the very good performance of the reconfiguration mechanism controller. This is shown in Figure 5.16.

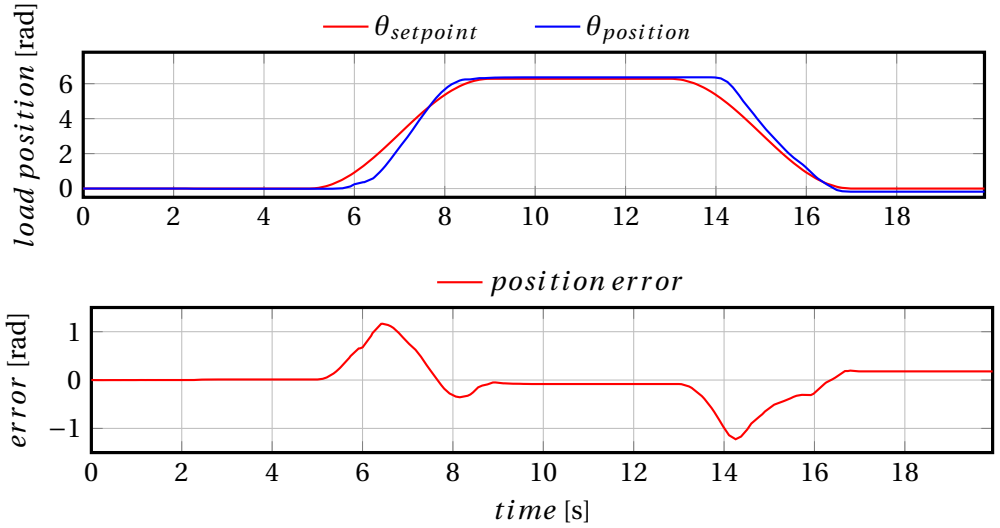

Figure 5.16: Position control using PID series controller with τ_i tunned for reconfiguration system. The plot shows the load position.

Finally, for the Parallel PID controller, it is possible to observe a very smooth behavior, just like the Series PID with τ_i tuned, nevertheless, still with a steady state error present in the final position of the load.

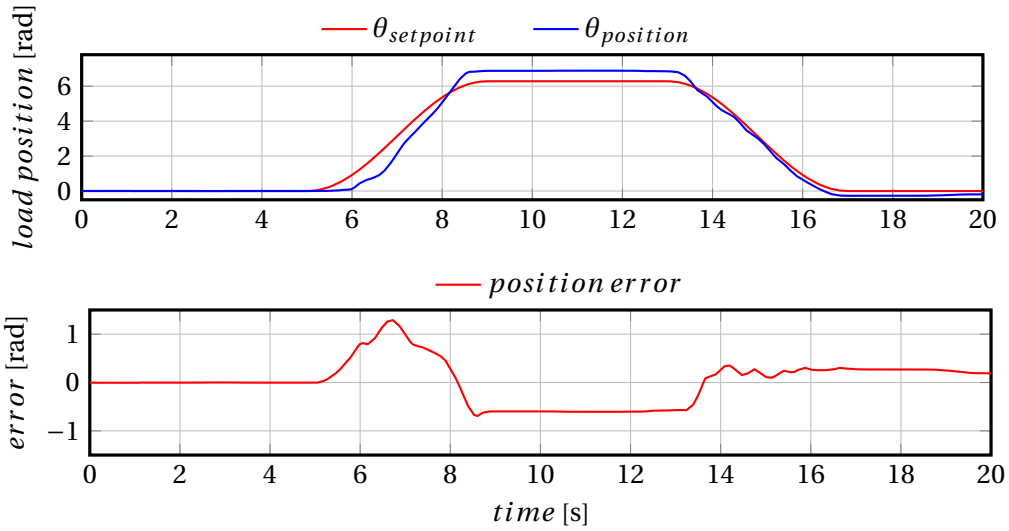

Figure 5.17: Position control using PID parallel controller for reconfiguration system. The plot shows the load position.

The position control experiment together with the ratio control experiment from Section 5.3, give a very good overview about the performance of the controllers. Overall, the adaptive feed forward controller combined with the Series PID has given the best results. In section 5.5, an analysis of the energy consumption for the reconfiguration mechanism with the different controllers is made, since the improvement of energy efficiency is the main goal of the ROSE project.

5.5 Energy consumption

In this section, an analysis for energy efficiency of the reconfiguration system is made, this, depending on the controller applied to the system just like in previous sections.

First a comparison of the torques generated during the ratio control is done. This is shown in Figure 5.18. It is possible to observe that the generated torques are very similar, thus it is not possible to determine if one controller leads to a better performance in energy efficiency terms.

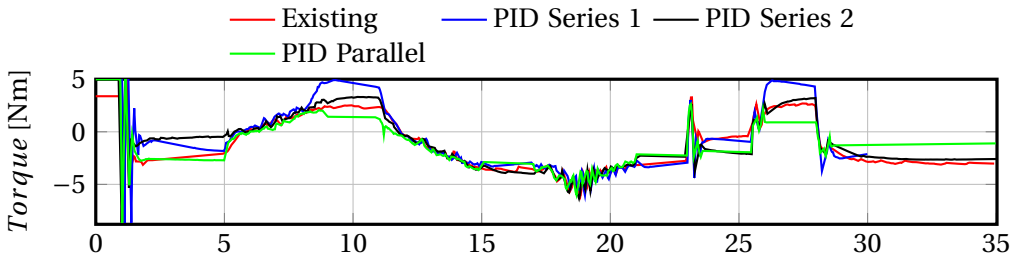

Figure 5.18: Torque comparison for ratio control

The same analysis for energy efficiency was performed in the position control experiment, where the torques generated by the four controllers are compared. This is shown in Figure 5.19. In this case, unlike the previous, it is possible to observe some differences. Specially in the Series PID 2 controller, the torque has more stable behavior (less fluctuations) and keeps value close to zero, which means less energy consumption compared to the other controllers.

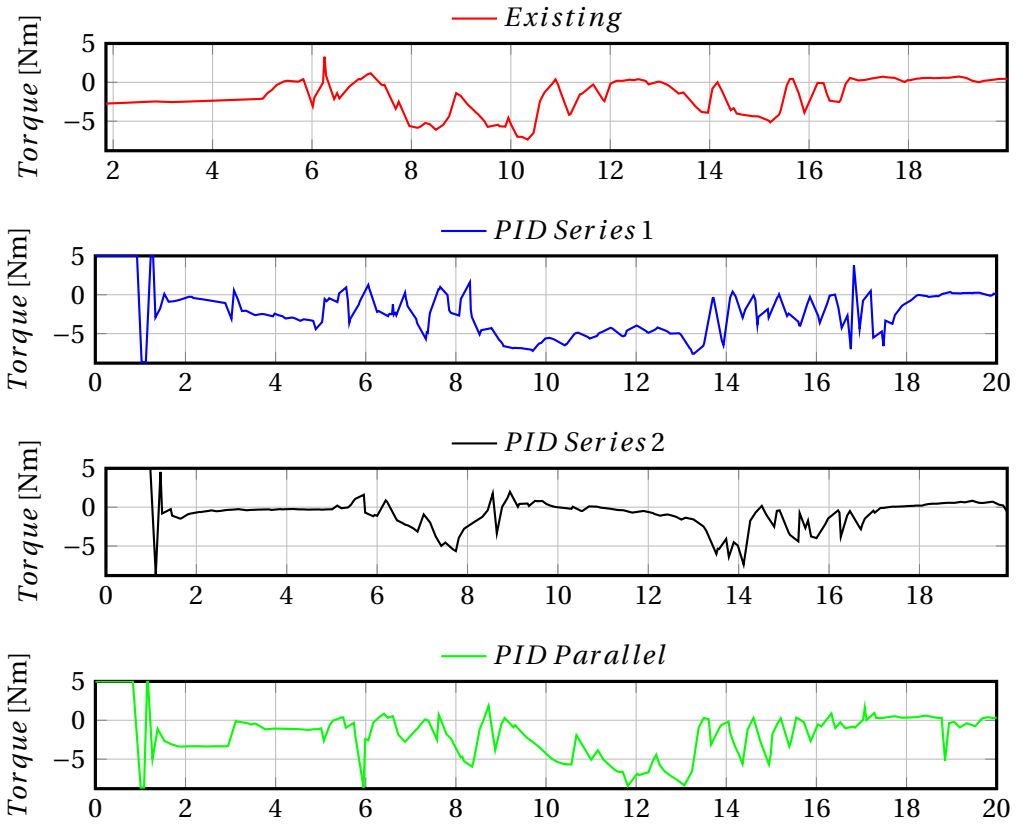

Figure 5.19: Torque comparison for position control

5.6 Controller selection

To summarize the results obtained in the experiments described in Sections 5.2, 5.3 and 5.4, Table 5.1 was generated. It is important to note that not all the experiments contribute equally to the selection criteria. Because of this, different weights are attributed to each of the tests. The step response, for example, doesn't provide information about the behavior of the controller

for all the positions inside the operational range, that is why this experiment has lower weight compared to the other two. The ratio control gives an idea of the behavior of the reconfiguration mechanism along all the operational range, nevertheless, this does not reassemble the standard operation mode. Because of this, the experiment receives less weight than the position controller. Finally, the most importance in the criteria is attributed to the position control experiment, because it tests the controller in the nominal conditions under which it is meant to work (controlled passive actuation).

Table 5.1: Comparison of controllers performance for different experiments.

Experiment	**Controller**				**Weight of experiment**
	Existing	**FF+Series PID 1***	**FF+Series PID 2**	**FF+Parallel**	
Step Response	++	–	+	-	✓
Ratio Control	–	++	+	-	✓✓
Load Position Control	-	–	++	+	✓✓✓
Selection	Series PID 2 with Feed Forward				

*Controller with unstable behavior for any of the experiments carried out.

In table 5.1, the **++** symbols were assigned to the controller with the best performance in the experiment, a **+** symbol to the second best, a **–** to the controller with the worst performance and a **-** to the controller in between the two previous cases. All in all, it is possible to observe that the best performance was obtained with the combination of the feed forward controller and the Series PID controller with τ_i tuned (Series PID 2). Furthermore, taking into account the results in Section 5.5, it is once again this combination, the one with the highest energy efficient behavior. The high gains at low frequencies of the Series PID 1 controller came out in the last experiment, causing unstable behaviors in the system.

6 Conclusions and Recommendations

6.1 Conclusions

The aim of this assignment was to design a controller for the reconfiguration mechanism of the Dual-Hemi CVT. The system's goal is to improve the energy efficiency of walking robots, by means of the controlled passive actuation (CPA) principle. The reason to focus on the controller for the reconfiguration mechanism is given by the fact that the CPA is heavily dependent on the performance of this mechanism. Therefore, having a good controller for this part of the Dual-Hemi CVT leads to a higher efficiency for the whole system.
Because of this, our research question turned into finding out which controller generates the best performance for the reconfiguration mechanism.

The modeling and design steps that were taken are chapter specific and were presented in chapters 3 and 4, respectively. The empirical findings were presented in Chapter 5. In synthesis, the results in each of these areas are given by:

- **Non-idealities Modelling:** After the identification of the friction and residual forces, they were represented in the model as a single element. This proved to be a good decision because, for the general purpose of this thesis, it was not necessary to investigate further the specific causes for each of the disturbances, but rather have an approximation of the total effect. Nevertheless, it is recommended to create separate models for the friction and residual forces, in order to compensate more accurately for the non idealities. For instance, as mentioned in section 3.3.1, a LuGre model for the friction forces is expected to resemble the effects of stiction, coulomb and viscous frictions.

- **Competence of the model:** Comparing the simulations with empirical findings, it was possible to determine that the level of detail of the obtained model was sufficiently competent for the purpose of this thesis (to design a controller based on this model).

- **Series PID 1 controller designed using the rules of thumb:** This controller obtained very good results in continuous time (simulations) for smooth changes in the reference path, however, in limited sample frequencies (discrete control) experiments, it showed unstable behavior. Basically, for this controller to perform as well as in the (continuous time) simulations, very high frequencies are required (3 times higher frequency compared to the other designed controllers).

- **Improving the results of the Series PID 1 controller:** By combining the tunings obtained using the rules of thumb with the insight from simulations with abrupt reference changes, it was possible to tune the controller based on the desired frequency response. This led to a stable behavior that kept the originally good performance (this controller is referred to as Series PID 2).

- **Final selection:** The chosen controller for the reconfiguration mechanism was the Series PID 2, as it presented the best performances in tracking error and response time as well as good ability to cope with the non-idealities of the system.

In this study it was possible to see the differences between the modelled ideal plant and the actual plant. In spite of the fact that the non-idealities were taken into account in our model, they were not compensated completely. By definition a model can never represent 100% the real system. This is why the evaluation of the model is given in terms of its competence to fulfill a purpose, otherwise the level of detail that can be reached is practically limitless. In our case, the goal was to design a controller based on this model. Because of this, a small adjustment to

the tunings given by of the rules of thumb, for this thesis, is an acceptable price to pay to save the considerable amount of time that a fully comprehensive model of the non-idealities or the implementation of a learning feed forward controller would have cost. All in all, after doing these adjustments, the results were very satisfactory and we were able to fulfill the requirement of improving the performance of the reconfiguration mechanism of the Dual-Hemi CVT.

6.2 Recommendations

As mentioned before, it is recommended to further develop the found friction model for the non idealities, so the feed forward controller is able to compensate, in a bigger measure, for the non idealities acting on the system. A separate model for the residual forces of the spring needs to be generated, which is expected to be linear or polynomial model.

Since the selected controller has a very good and reliable behavior, it is advise to use a similar approach for the improvement of the force-position controller of the Dual-Hemi CVT. The model developed in Section 3.1, can serve as a start for this procedure, since the values for all the components have been already calculated.

A Appendix 1

A.1 Dual-Hemi CVT elements' detail

Element	Value
Motor (as source of Torque) T	-
Motor inertia I_m	$2.12\times10^{-6}\ kgm^2/rad$
Motor shaft stiffness	$480.4617\ Nm/rad$
Inertia of gear mounted on motor shaft I_{prg}	$4.34\times10^{-8}\ kgm^2/rad$
i_1	$6.3 \quad mm$
Belt drive transformer (the belt stiffness) C_{tb}	$5296000\ N/m$
i_2	$1/28.27 \quad 1/mm$
Inertia of secondary gear I_{scg}	$5.226\times10^{-6}\ kgm^2/rad$
Rotational stiffness of the arm to fix the outer part of the clock spring	$29.275\times10^{6}\ Nm/rad$
Inertia of the arm to fix the outer part of the clock spring I_{scl}	$6.616\times10^{-5}\ kgm^2/rad$
Stiffness of the clock spring K_{cs}	$0.33062\ Nm/rad$
Inertia of safety clutch + shaft + sun gear I_{sng}	$1.8823\times10^{-5}\ kgm^2/rad$
i_3	$7.925 \quad mm$
Stiffness between teeth of sun and planet gears	∞
i_4	$1/10 \quad 1/mm$
Inertia of planet gears I_{ptg}	$3.693\times10^{-6}\ kgm^2/rad$
i_5	$10 \quad mm$
Stiffness between teeth of ring and planet gears	∞
i_6	$1/28.15 \quad 1/mm$
Inertia of the carrier (cage) I_{cage}	$2.7255\times10^{-5}\ kgm^2/rad$
Inertia of the ring gear I_{rgg}	$1.1663\times10^{-4}\ kgm^2/rad$
Stiffness of shaft from ring gear to crown gear$_1$	$17766.638\ Nm/rad$
Inertia of crown gear$_1$ I_{cng1}	$1.2021\times10^{-4}\ kgm^2/rad$
i_7	$30.25 \quad mm$
Stiffness between teeth of gears	∞
i_8	$1/31.413 \quad 1/mm$
Inertia of spur gear$_1$ + sphere$_1$ + its shaft I_{sp1}	$1.5841\times10^{-3}\ kgm^2/rad$
CVT with unknown stifness and variable transmission ratio	-
Inertia of spur gear$_2$ + sphere$_2$ + its shaft I_{sp2}	$1.5745\times10^{-3}\ kgm^2/rad$
i_9	$31.413 \quad mm$
Stiffness between teeth of gears	∞
i_{10}	$30.25 \quad 1/mm$
Inertia of crown gear$_2$ I_{cng2}	$1.2778\times10^{-4}\ kgm^2/rad$
Stiffness of shaft from crown gear$_2$ to spur gear$_3$	$362.368\ Nm/rad$
Inertia spur gear$_3$ I_{spg3}	$4.891\times10^{-4}\ kgm^2/rad$
i_{11}	$60.5 \quad mm$

Table A.1: Elements that form the DH-CVT and its values

Element	**Value**
Stiffness between teeth of gears	∞
i_{12}	$1/60.5 \quad 1/mm$
Inertia of spur gear that connects to cage I_{gcg}	$1.1685\times10^{-3}\ kgm^2/rad$
i_{13}	$60.5 \quad mm$
Stiffness between teeth of gears	∞
i_{14}	$1/60.5 \quad 1/mm$
Inertia of spur gear output + output shaft I_{gout}	$5.2974\times10^{-4}\ kgm^2/rad$
Stiffness of output shaft	$47909.287\ Nm/rad$
Load I_{load}	-

Table A.1: Elements that form the DH-CVT and its values

A.2 Reconfiguration mechanism elements' detail

Element	**Value**
Motor (as source of Torque) T	-
Motor inertia I_m	$2.12\times10^{-6}\ kgm^2/rad$
Gearbox ratio	1:35
Gearbox Inertia I_{gb}	$1.7692\times10^{-7}\ kgm^2/rad$
Belt drive input ratio	$6.9\ \ mm$
Timing belt stiffness C_{tb}	$7500000\ N/m$
Belt drive input ratio	$1/28.22\ \ 1/mm$
Inertia of secondary gear of belt drive	$3.45035\times10^{-6}\ kgm^2/rad$
Length of lever	$120\ mm$
Mass of mobile sphere module M_{sph}	$4.5\ kg$
Stiffness of gravity compensator spring C_{gc}	$1800\ N/m$
Rolling friction between spheres R_s.	3.2
Force due to gravity F_{mg}	$M_{sph}\times g\times length\ of\ lever\times\cos(\theta_r)$

Table A.2: Elements that form the reconfiguration mechanism and its values

B Appendix 2

B.1 Soft initialization for DH-CVT

It is desired to avoid overshoot due to the abrupt change in the set-point at the beginning of the experiments in the Dual Hemi CVT. Because of this, a modification to the to the homing sequence was made. In this, instead of using the calculation of a cycloid to control the torque fed to the reconfiguration system motor, a path with a sine wave like signal was put as a reference for the controller, giving enough time to make a smooth transition to the initial position of the experiments ($transmission\ ratio = 0$). The results are shown in Figure B.1, where we can observe that using the Series PID 1 controller generates no overshoot, thanks to the new homing procedure. In Figure B.2 it is possible to observe the behavior of the reconfiguration mechanism for whole experiment.

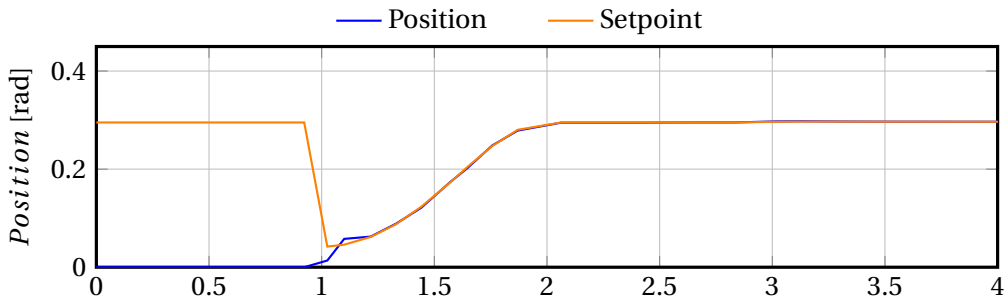

Figure B.1: Soft transition to initial position in experiments.

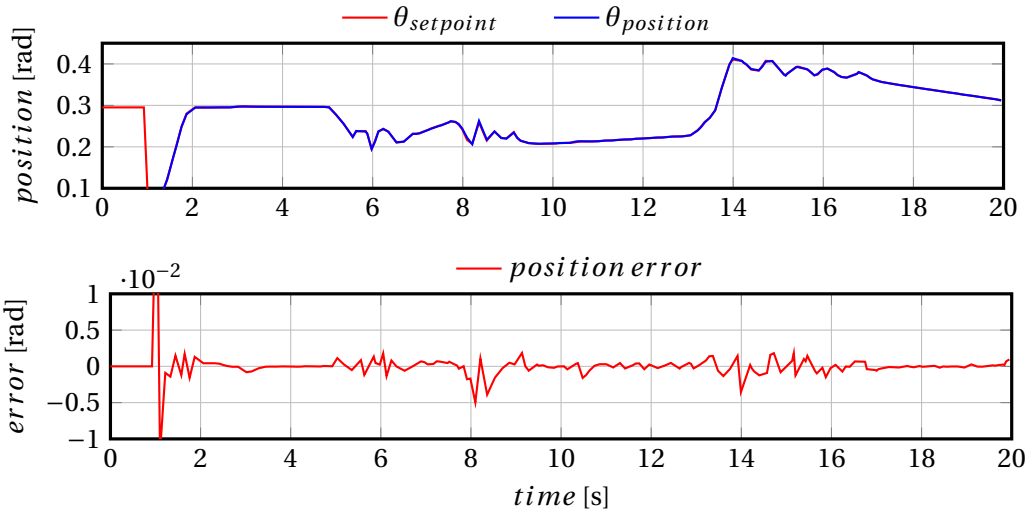

Figure B.2: Position control using PID Series 1 with soft initialization. The plot shows the position of the reconfiguration mechanism.

Bibliography

[1] M. Naves, "Design of a continuously variable transmission for efficiently actuating walking robotic sensors." University of Twente, 2015.

[2] D. Dresscher, M. Naves, T. J. de Vries, M. Buijze, and S. Stramigioli, "Power split based dual hemispherical continuously variable transmission." University of Twente, 2016.

[3] E. Coeling, T. J. A. de Vries, and M. P. Koster, "Assessment of mechatronic system performance at an early design stage," *IEEE Transaction on Mechatronics*, pp. 269.1–279.1, Vol. 7, nr. 3, September 2002, 2002.

[4] A. Macchelli, "Port hamiltonian systems. a unified approach for modeling and control finite and infinite dimensional physical systems," Ph.D. dissertation, Ph. D. dissertation, University of Bologna–DEIS, 2003, available at http://www-lar. deis. unibo. it/woda/spider/e499. htm, 2003.

[5] J. van Amerongen and P. Breedveld, "Modelling of physical systems for the design and control of mechatronic systems," *Annual reviews in control*, vol. 27, no. 1, pp. 87–117, 2003. [Online]. Available: http://doc.utwente.nl/74874/

[6] D. de Roover, *Motion control of a wafer stage: a design approach for speeding up IC production*. Delft University Press, 1997. [Online]. Available: https://books.google.nl/books?id=w9VSAAAAMAAJ

[7] T. McGeer, "Passive dynamic walking." *I. J. Robotic Res.*, vol. 9, no. 2, pp. 62–82, 1990. [Online]. Available: http://dblp.uni-trier.de/db/journals/ijrr/ijrr9.html#McGeer90

[8] R. Tedrake, T. W. Zhang, M. fai Fong, and H. S. Seung, "Actuating a simple 3d passive dynamic walker." in *ICRA*. IEEE, 2004, pp. 4656–4661. [Online]. Available: http://dblp.uni-trier.de/db/conf/icra/icra2004-5.html#TedrakeZFS04

[9] S. H. Collins, M. Wisse, and A. Ruina, "A three-dimensional passive-dynamic walking robot with two legs and knees." *I. J. Robotic Res.*, vol. 20, no. 7, pp. 607–615, 2001. [Online]. Available: http://dblp.uni-trier.de/db/journals/ijrr/ijrr20.html#CollinsWR01

[10] D. Dresscher, T. J. de Vries, and S. Stramigioli, "Spring-Driven Controlled Passive Actuation." University of Twente, 2016.

[11] Mechanical, Industrial and Technical Calculations, "Springs calculation," 2016. [Online]. Available: http://www.mitcalc.com/

[12] T. de Vries, *Mechatronic Design of Motion Systems*. Robotics and Mechatronics, Utwente, 2014.

[13] F. Bottiglione and G. Mantriota, "Reversibility of power-split transmissions." vol. 133, 2011, pp. 084 503–1–084 503–5.

[14] R. Merzouki, A. K. Samantaray, P. M. Pathak, and B. O. Bouamama, *Intelligent Mechatronic Systems: Modeling, Control and Diagnosis*. Springer Publishing Company, Incorporated, 2012.

[15] R. J. Ferguson, "Shortcuts for analyzing planetary gearing," *Machine Design*, pp. 55–58, 1983.

[16] B. CO., "Polyurethane timing belts," p. 142. [Online]. Available: http://www.brecoflex.com/download/B212.PDF

[17] I. Virgala and M. Kenderová, Peter Frankovsky, "Friction effect analysis of a dc motor," *American Journal of Mechanical Engineering*, vol. 1, no. 1, pp. 1–5, 2013. [Online]. Available: http://pubs.sciepub.com/ajme/1/1/1

[18] H. Olsson, K. J. Åström, M. Gäfvert, C. C. D. Wit, and P. Lischinsky, "Friction models and friction compensation," *Eur. J. Control*, p. 176, 1998.

[19] C. C. de Wit, H. Olsson, K. J. Astrom, and P. Lischinsky, "A new model for control of systems with friction," *IEEE Transactions on Automatic Control*, vol. 40, no. 3, pp. 419–425, Mar 1995.

[20] H. Olsson, "Control systems with friction," p. 172, 1996.

[21] A.-J. Annema, *Feed-Forward Neural Networks, Vector Decomposition Analysis, Modelling and Analog Implementation*. MESA Research Institute, Utwente, 1995.

[22] K. Åström and B. Wittenmark, *Adaptive Control: Second Edition*, ser. Dover Books on Electrical Engineering. Dover Publications, 2013. [Online]. Available: https://books.google.nl/books?id=4CLCAgAAQBAJ

[23] N. S. Nise, *Control Systems Engineering*, 3rd ed. New York, NY, USA: John Wiley & Sons, Inc., 2000.

[24] A. O'Dwyer, *Handbook of PI and PID Controller Tuning Rules*. Imperial College Press, 2009. [Online]. Available: https://books.google.nl/books?id=zivrLUbIMgUC